FORM TI-12
08/2007

B-T-3613

In-situ Fracture Studies and Modeling of the Toughening Mechanism Present in Wrought LCAC, TZM, and ODS Molybdenum Flat Products

B.V. Cockeram[(1)], and K.S. Chan [(2)],

[(1)]Bechtel-Bettis Atomic Power Laboratory, P.O. Box 79, West Mifflin, PA 15122-0079
[(2)]Southwest Research Institute, San Antonio, TX 78238

BECHTEL BETTIS, INC. WEST MIFFLIN, PENNSYLVANIA 15122-0079

In-situ Fracture Studies and Modeling of the Toughening Mechanism Present in Wrought LCAC, TZM, and ODS Molybdenum Flat Products

B.V. Cockeram[(1)], and K.S. Chan[(2)]

[(1)]Bechtel-Bettis Atomic Power Laboratory, P.O. Box 79, West Mifflin, PA 15122-0079,

[(2)]Southwest Research Institute, San Antonio, TX 78238.

Abstract

In-situ testing, ultrasonic C-scans, and metallography were used to show that a crack-divider delamination form of thin-sheet toughening occurs in wrought Low Carbon Arc Cast (LCAC) unalloyed molybdenum, Oxide Dispersion Strengthened (ODS) molybdenum, and TZM molybdenum at temperatures ≥ the Ductile to Brittle Transition Temperature (DBTT). Cracking along boundaries relieves mechanical constraint to free ligaments that may plastically stretch to produce toughening. Anisotropy in fracture toughness with lower values in the short-transverse direction is shown to produce the crack divider delaminations at the crack tip in the LT and TL orientations. The delamination zone increases with increasing stress-intensity to sizes significantly larger than the plastic zone, which leads to large increases in fracture toughness by the thin sheet toughening mechanism. Fracture in ODS Mo-alloys proceeds mainly along grain boundaries to produce small ligaments that exhibit ductility for both LT and TL orientations resulting in a lower DBTT and higher toughness values at lower temperatures than observed in LCAC and TZM. A combination of grain boundary fracture and cleavage is prevalent in LCAC molybdenum and TZM. The predominance for microcracking along grain boundaries to leave fine, ductile ligaments in ODS molybdenum can be attributed to a fine-grained microstructure with ≈1-2 μm thickness of sheet-like grains. The presence of mixed grain boundary fracture and cleavage in LCAC and TZM can be attributed to a microstructure with a larger thickness of sheet-like grains (4 - 15 μm).

I. INTRODUCTION

Molybdenum alloys are used in applications where high-temperature strength and creep resistance are needed, but poor oxidation resistance limits their use to applications where a controlled atmosphere can be maintained [1-4]. Molybdenum has a body-centered cubic (bcc) structure and, like the majority of bcc metals, exhibits a Ductile to Brittle Transition Temperature (DBTT). Also, its fracture properties are sensitive to temperature [5], interstitial content [5], grain size [5,6], slip or deformation mechanisms [7-9], grain boundary character [10-13], and microstructure [14-25]. Studies of molybdenum alloys generally have used unnotched tensile or bend specimens, where large amounts of ductility typically are measured near a homologous temperature of 0.1 (≈17°C) or greater to define the DBTT. Recent work has shown that the use of fracture toughness testing results in a higher DBTT (100°C to 200°C) than obtained from tensile specimens for both wrought unalloyed Low Carbon Arc Cast (LCAC) molybdenum and a wrought molybdenum alloy with 0.5% Ti and 0.1% Zr additions by weight (TZM). This can be ascribed to the constraining effect of the pre-crack [14-16]. Higher fracture toughness values at lower temperatures and lower toughness based DBTT values are observed for wrought molybdenum alloys that have a finer grain size, such as Oxide Dispersion Strengthen (ODS) molybdenum [14-16]. The wrought LCAC, TZM, and ODS molybdenum alloys used in these studies have microstructures consisting of elongated, pancake shaped grains. These recent studies [14-16] have shown that one of the fracture mechanisms in wrought molybdenum-based alloys involves the formation of thin sheet ligaments [27, 28] that leads to an enhancement of the fracture resistance of Mo-Based alloys [14-16] via a ductile-laminate toughening mechanism similar to that observed for Al-based alloys [27-29], steels [30], lamellar TiAl-based alloys [31], and metal-matrix composites [32]. The overall material toughness goes up because fracture at the grain boundaries allows the grain interiors to deform more freely, thereby increasing the plastic energy absorbed by the material prior to complete crack propagation across the sample.

The enhancement in fracture toughness that results from thin sheet toughening is produced by relaxing the triaxial stresses near the crack tip and increasing the critical strain at fracture [27, 28]. The theoretical maximum increase in fracture toughness that can be achieved through thin sheet toughening has been estimated to be a factor of $\sqrt{3}$ [27-28], but higher levels of fracture toughness enhancement have been obtained in ODS, LCAC, and TZM molybdenum [14-16]. This apparent discrepancy can be attributed to an increase in the process zone size at the crack tip due to a crack-divider delamination [26, 27]. There is, however, little information on the critical conditions that govern crack-divider delamination, the evolution of the delamination process zone, and the role of microstructure on the delamination process in Mo-based alloys.

The objectives of this study are to characterize the fracture resistance, crack-divider delamination, and the fracture mechanisms for wrought ODS, LCAC, and TZM molybdenum alloys [14-16]. In-situ fracture toughness testing was performed in a Scanning Electron Microscope (SEM) and near-tip strain distribution measurements were made to clarify the fracture mechanism. Non-destructive ultrasonic techniques were used to evaluate the development of internal delamination at the crack-tip. These experimental results were utilized in the development of a mechanical model to describe crack-divider delamination and the microstructure/fracture property relationship in the molybdenum-base alloys.

II. EXPERIMENTAL PROCEDURES

A. *Materials and Specimen Preparation*

The LCAC, TZM, and ODS molybdenum were obtained from H.C. Starck, Cleveland, OH as 9.53 mm (LCAC) or 6.35 mm thick wrought plate in the stress-relieved condition [14-16]. These are the same heats used in previous testing [14-16]. The processing chemistry, and microstructures of these alloys are described in Table I. The microstructures consist of sheet-like, pancake-shaped grains that are aligned in the longitudinal orientation. ODS molybdenum also contains 2 volume% La-oxide particles that are both aligned in the longitudinal orientation as ribbons and dispersed as fine particles. This results in a finer sheet-like grains [33,34].

Compact-tension (CT) specimens (19.8 mm in width, 19.1 mm in height, and 4.8 mm in thickness [35]) were fabricated using electrode-discharge machining with the notch/crack in either the LT (longitudinal) or TL (transverse) orientation [36]. After machining, all specimens were mechanically polished to a surface finish of approximately 0.05 μm. The specimens were fatigue-precracked at ambient temperature (25°C) under compression/compression cyclic loads at 10-15 Hz using ASTM procedures as a guide [37,38]. The maximum stress intensity factor was computed by treating the specimen as a single-edge crack in uniform compression [39] and was nominally 45 MPa$\sqrt{m}$ for each specimen. The pre-cracking was performed with a load ratio, R, of 0.04-0.06 for 37,000 to 4,890,000 cycles to produce an a/W ratio ranging from 0.52 to 0.60. After fatigue precracking, the test specimens were ion-etched in an ion sputter system operated at 8 KeV, 3.8×10^{-6} torr pressure, under an Argon beam for 30-60 minutes to reveal the microstructure and to condition the surfaces for imaging in the SEM [35].

B. *Testing Procedures*

In-situ fracture toughness tests were performed in a SEM equipped with a high-temperature loading stage [40]. Tensile loads were applied to the specimen and the stress intensity factors (K) were computed using the boundary-correction function described in ASTM-E399 [41]. A summary of the specimens and test conditions is presented in Table II. Ultrasonic C-scans were performed on the pre-cracked specimens and after loading to various K levels to detect internal delaminations and track the evolution of the delaminations. The ultrasonic waves were generated by a 25 MHz, 6.35 mm diameter focused transducer with a focal length of 38.1 mm in ambient water. The transducer was positioned above the samples so that the focal point was located in the middle of the sample width and a 5 mm by 5 mm region was scanned at the crack tip. The transducer was used in the pulse-echo mode, where the transducer that generates the ultrasonic waves also receives the reflected waves. The transducer was powered by a 300-volt pulse from a UTEX UT340 pulser/receiver. The reflected signals from the transducer were amplified by a 9 dB amplifier in the UT340 instrument. The waveforms were

digitized by a digital analog/digital converter at a 250 MHz sampling rate and were stored in a PC for post-examination analysis of the defect area with an estimated resolution of 25 μm.

Prior to fracture testing, reference photographs of the near-tip region were obtained under a small load (90 N). The tensile load was applied to increase the K in 5 MPa $\sqrt{m}$ increments starting at K =10 MPa $\sqrt{m}$. A maximum K level of 50 to 70 MPa $\sqrt{m}$ was used, depending on the alloy and test temperature. The $K_{Tensile}$ in the notch-tip computed on the basis of the compression/compression fatigue load cycle was about 13 MPa $\sqrt{m}$ for each individual specimen. The expression for $K_{tensile}$ ($K_{Tensile} = \frac{1}{\sqrt{3}}\left(\frac{\Delta K}{2}\right)$), where ΔK is the stress intensity range of the compression/compression fatigue cycle under the plane strain condition, was derived by considering the tensile stress induced in the notch plastic zone during a compression/compression fatigue cycle. At a given K level, still photographs near the near-tip region were taken and the corresponding crack extension (Δa) was measured directly from the near-tip images. This process was then repeated at a higher K level until the fracture test was interrupted at selected K levels. Micrographs of the same near-tip region at the unloaded and loaded conditions constitute a stereo-pair that were analyzed using a vision-based stereoimaging technique that measures the displacement and strain field near the crack tip [42,43]. SEM fractography was performed on several specimens that fractured during in-situ fracture testing before the entire series of K levels was applied. Seven specimens remained intact after in-situ fracture testing to K levels of 32 – 70 MPa $\sqrt{m}$. To verify the ultrasonic C-scan results, the intact CT specimens were sectioned along the vertical plane at the crack tip and then polished and etched using metallographic techniques and given Murakami's etch (10g Potassium Ferri-cyanide + 10g Potassium Hydroxide + 100 ml water).

III. Results

A. *In-situ Toughness Test Results*

The K-resistance curves for LCAC and TZM determined from in-situ fracture testing are shown in Figure 1 to exhibit an initiation toughness ranging from 30 to 69.2 MPa $\sqrt{m}$ followed by unstable crack extension at a constant K level. One test of LT LCAC at 200°C did not result in any crack extension after loading to a K level of 70 MPa $\sqrt{m}$. This indicates that the fracture toughness is greater than 70 MPa $\sqrt{m}$ under these conditions. The K-resistance curves for ODS are shown in Figure 2 to exhibit stable crack extension with increasing K after K levels of about 10 to 40 MPa $\sqrt{m}$, and maximum K levels of 32-65 MPa $\sqrt{m}$ are achieved without unstable crack extension being observed. Large crack extension without fracture was observed for one TL-ODS specimen tested at 150°C at a K of 50.2 MPa $\sqrt{m}$, suggesting that the critical K for unstable crack growth was 50.2 MPa $\sqrt{m}$ in this case. The DBTT for ODS is lower than LCAC and TZM (Table I). That may explain, in part, why stable crack extension was observed for ODS molybdenum at lower temperatures (25°C-150°C) than for LCAC and TZM (100°C-200°C).

Table II presents a summary of the critical K_c values for unstable crack extension observed for 6 of the 12 specimens. The other six specimens did not fracture, and no crack formation or stable crack extension was observed after testing to the maximum K levels shown in Table II. Therefore, the K_c value for unstable crack growth was assumed to be higher than the measured values for these samples. It should be noted that none of the tests met the ASTM requirements for a valid fracture toughness test [44] as the plane strain conditions for specimen thickness ($a \geq 2.5 (K_Q / \sigma_y)^2$) were not satisfied for any of the tests. The K_c values determined from these in-situ tests (Table II) generally were within the range of respective fracture toughness values previously determined for LCAC, TZM, and ODS at temperatures > DBTT (Table I). Three exceptions are in the case of LT-TZM, LT-LCAC, and TL-ODS where the K_c values were slightly lower than the previous range by values of 3 to 19 MPa $\sqrt{m}$. All K_c results were above the 30 ± 3 MPa $\sqrt{m}$ minimum value used to define the DBTT, consistent with the

reported DBTT values for these materials. In the case of TL-LCAC tested below the DBTT at 150°C, fracture occurred at a K_c of 27.8 MPa$\sqrt{m}$. This also is consistent with the reported DBTT. These tests were performed at temperatures close to or equivalent to the DBTT where scatter in fracture toughness values would be expected. The K_c results may represent new lower bound toughness values but more data needs to be obtained. Interruption of the tests and exposure of the crack-tip to water during the C-scans may also result in a slightly lower toughness compared to previous results although in-situ fracture information still is obtained.

B. *In-situ Observations for ODS Molybdenum*

The near-tip fracture processes for LT and TL-ODS are shown in Figures 3 and 4, respectively. Failure proceeds by the development of microcracks along grain boundaries perpendicular to the main crack plane in the process zone leaving ligaments of intact grains that are stretched to failure as the main crack extends at higher K levels. There is a tendency for the main crack to deflect along vertical grain boundaries for LT-ODS and travel out-of-plane and parallel to the applied stress axis, while a sharp crack is observed for TL-ODS that travels in a direction perpendicular to the stress direction. The anisotropy in microstructure and toughness values for ODS with grains and oxide particles aligned in the longitudinal orientation is consistent with the direction that cracks growing in the LT orientation tend to propagate out-of-plane towards the TL orientation [14-16]. A plot of near-tip strain distributions for LT-ODS in Figure 5a shows that the near crack-tip effective strain approaches 40% at a distance of 1 μm from the crack-tip and then decreases with increasing distance from the crack tip. The near-tip strain distributions for TL-ODS are shown in Figure 5b to be comparable and insensitive to the applied K level. This implies the presence of one or more shielding mechanisms that reduce the local stress intensity factor at the crack tip.

Images of the ultrasonic C-scans performed at the crack tip for LT and TL-ODS at increasing K levels show in Figures 6 and 7, respectively, that internal delamination zones are formed at the crack-tip in the region of the plastic zone. The delamination zones are depicted in

colors of yellow to red with red signifying a higher level of delamination. Regions without delamination are shown in blue. In general, the size of the internal delamination zones increase as the applied K levels are increased. These C-scan results show that delaminations are formed in ODS in the region of triaxial stress-state at the crack-tip. This leaves thin ligaments of grains that can be stretched to failure under plane stress conditions to provide toughening by the thin-sheet mechanism [14-16, 26,27]. The thickness of the delamination zones determined from the C-scan inspections was confirmed by metallographic examinations near the crack tip, see Figure 8. Large delamination cracks can be seen at lower magnifications (Figures 8a and 8c), but smaller linear microcracks on the order of 5-50 μm in length are present in the ligaments between the larger delamination cracks (Figures 8b and 8d). These smaller cracks appear to propagate along the grain and oxide boundaries, but it was difficult to differentiate clearly between the small cracks and boundaries in these examinations. The fine ligaments observed at ODS fracture surfaces in previous work are on the order of the same thickness as the grains [14-16], indicating that microcracking along individual grain/oxide boundaries to leave thin ligaments is the process that controls the fracture of ODS molybdenum (Figure 8e). Table III shows that the delamination zones in LT and TL-ODS are about 7-13 times larger than the respective plastic zones. The experimental plastic zone size was determined as the distance from the crack to where $\bar{\varepsilon}_{\text{eff}}$ = .5% in the near-tip effective strain distributions for individual specimens. A constant process zone size was computed as $h = n^2 r_o$, by assuming n = 0.035 and r_o = 0.06 m.

C. *In-situ Observations for LCAC and TZM Molybdenum*

The crack growth processes, near-tip effective strain distributions, and fracture surfaces for TZM in the LT and TL-orientations tested at 100°C and 150°C, respectively, are shown in Figure 9. C-scans of crack-tips are shown in Figure 10. The formation of microcracks in ODS (Figures 3 and 4) and slip bands in LCAC (Figures 11 and 12) are observed at the crack-tip prior to crack extension, but neither of these features are observed at the crack-tip for TZM.

Both TZM and LCAC were tested at near DBTT temperatures where unstable crack extension to failure was observed at a critical K value. A bridging ligament is shown in Figure 9a for LT-TZM, and ductile ligaments are observed at the fracture surface (Figure 9d). This indicates that the thin sheet toughening mechanism does play a role for these conditions. Cleavage also is observed on the fracture surfaces of TZM. Examination of the cleavage facets in stereo-pairs revealed that the facets are inclined to the stress axis, suggesting that cleavage might have occurred on a plane that could be a slip plane as part of the fracture process. Although LT and TL-TZM were tested at slightly different temperatures and to different K levels, the strain distributions shown in Figure 9c appear similar with a maximum near-tip strain of 15-25%. Ultrasonic C-scans show in Figure 10 that a small delamination zone was developed in TZM after pre-cracking and that the delamination zone was observed to increase with increasing K-levels for both orientations. The delamination zones for TZM are shown in Table III to be about a factor of 13 to 17 larger than the plastic zone.

Micrographs of the crack extension processes for LT and TL-LCAC are shown in Figures 11and 12. They are characterized by the formation of a slip line at the crack tip prior to unstable extension of the crack in both cases. The near crack-tip strain values for LCAC were in the range of 10% to 30% (Figure 13), and the plastic zone size for LCAC was similar to that observed for ODS and TZM. Small delamination zone sizes were observed for LT and TL-LCAC (Figure 14). In fact, delaminations could not be resolved using C-scans for two of the four specimens tested. In one case where crack extension did not occur for LT-LCAC tested at 200°C, delaminations were not resolved in the C-scan in Figure 14f and cracks could not be detected by metallographic sections near the crack tip (Figure 15c). However, a mixed-mode failure consisting of cleavage facets and ductile laminates was observed for TL and LT-LCAC (Figure 15). Cleavage facets were prevalent in some cases and examinations of stereo-pairs showed that the cleavage facets were inclined to the stress axis, which suggests that cleavage occurred on a plane that could be a slip plane. These results suggest that slip bands are

formed at a K value slightly lower than K_c and that cleavage cracks are along the slip bands formed at the crack tip. Although delaminations could not be resolved at the crack tip using the C-scans or metallography, the fact that ductile laminate features were observed on the fracture surfaces indicates that thin sheet toughening is an important toughening mechanism for LCAC. It is likely that delamination zones always are present in LCAC, but are either sometimes too small or form as part of the fracture process at higher K levels.

Both ODS and TZM exhibit fracture controlled by the formation of delaminations at the crack-tip, but TZM exhibited a higher fraction of cleavage. These observations suggest that a finer grain size (ODS) results in a fracture that occurs by cracking along boundaries ahead of the crack tip with the development of a large delamination zone at the crack tip, and R-curve like behavior is observed (Figure 2). Delaminations were also observed for LCAC molybdenum, but the formation of slip lines were observed at the crack tip at higher K levels prior to unstable crack extension. Cleavage at the fracture surfaces for TZM and LCAC was much more prevalent than observed for ODS, which may be explained by the larger grain size of TZM and LCAC. When the grains are large the laminate spacing is also large. The spacing between barriers to slip is large. The observed slip band formation can result in the development of high stresses at dislocation pile-ups blocked at grain boundaries, and the initiation of cleavage cracks. A smaller delamination zone is developed for larger grained LCAC, and a higher fraction of cleavage is observed. TZM is an intermediate case where the grain size is larger than ODS but smaller than LCAC. Long slip bands are not resolved at the crack tip but a delamination zone was developed. The development of a micromechanical model is pursued in the following section to clarify the role of microstructure on the fracture process.

IV. DEVELOPMENT OF MECHANICAL MODEL FOR FRACTURE BEHAVIOR

A. *Crack-Divider Delamination*

A micromechanical model is developed to describe the crack-divider delamination mechanism and its impact on thin-sheet toughening and fracture resistance of Mo-based alloys,

see Figure 16. A Mode I crack in a plate of thickness t is subjected to a remotely applied stress, σ, under the plane strain condition and results in principle stresses, σ_{33}, in the thickness (t) direction given by the following for a material with isotropic linear elastic behavior

$$\sigma_{33} = \nu\left(\sigma_{11} + \sigma_{22}\right) \tag{1}$$

where ν is Poisson's ratio, σ_{11}, and σ_{22} are the principal stresses in the plastic zone. Assuming the plastic constraint stresses are relaxed by forming a series of parallel, penny-shaped microcracks along weak interfaces (Figure 16), the elastic stress (σ_{mc}) and strain (ε_{mc}) for the formation and opening of the microcracks can be defined

$$\sigma_{mc} = -E\varepsilon_{mc} \tag{2}$$

which relaxes the constraint stress in the thickness direction (z)

$$\sigma_{33} = \nu\left(\sigma_{11} + \sigma_{22}\right) - E\varepsilon_{mc} \tag{3}$$

By treating individual microcracks as a penny-shaped crack, the strain is given as

$$\varepsilon_{mc} = \frac{n_c \delta_c}{t} \tag{4}$$

where n_c and δ_c are the number and the crack opening displacement of crack-divider delamination microcracks over the thickness (Figure 16a). For a penny-shaped crack subjected to static loading [45],

$$\delta_c = \frac{16(1-\nu^2) l \sigma_{33}^o}{3\pi E} \tag{5}$$

with

$$\sigma_{33}^o = \nu(\sigma_{11} + \sigma_{22}) \tag{6}$$

where *l* is the radius (r_d) of the penny crack (Figure 16) and σ_{33}^o is the constraint stress prior to delamination. Substituting Eqs. (4)-(6) into Eq. (3) gives

$$\sigma_{33} = \sigma_{33}^o - \frac{16 n_c (1-\nu^2) l \sigma_{33}^o}{3\pi t} \tag{7}$$

leading to

$$\frac{\sigma_{33}}{\sigma_{33}^{o}} = 1 - \frac{16(1-\nu^2)}{3\pi}\chi \tag{8}$$

with χ defined as the delamination crack density parameter

$$\chi = \frac{n_c l}{t} \tag{9}$$

Eq. (8) gives the relation between constraint stress relaxation and χ, where full constraint of the crack tip is defined as $\chi = 0$ and $\sigma_{33}/\sigma_{33}^{0} = 1$. The constraint stress, σ_{33}, decreases with increasing χ and σ_{33} becomes zero (fully relaxed) when χ reaches a critical value of

$$\chi_c = \frac{3\pi}{16(1-\nu^2)} \tag{10}$$

and has a value of $\chi_c = 0.65$ for $\nu = 1/3$. A stress state parameter is also defined from Eq. (8)

$$\eta = \frac{\sigma_{33}}{\sigma_{33}^{o}} \tag{11}$$

that has a value of 1 for the plane strain condition and a value of 0 for the plane stress condition. In terms of this stress state parameter, σ_{33} can be expressed in general as

$$\sigma_{33} = \eta\nu\left(\sigma_{11} + \sigma_{22}\right) \tag{12}$$

For a Mode I crack, the stresses in the crack plane and ahead of the crack tip are as follows

$$\sigma_{11} = \frac{K_I}{\sqrt{2\pi r}};\ \sigma_{22} = \frac{K_I}{\sqrt{2\pi r}} \tag{13}$$

These can be combined with Eq. (12) to give

$$\sigma_{33}\sqrt{\pi r} = \sqrt{2}\eta\nu K_I \tag{14}$$

leading to the following relationship for stress-intensity

$$\frac{K_{mc}}{K_I} = \sqrt{2}\eta\nu \tag{15}$$

where K_{mc} is the K factor of the crack–divider delamination microcrack as $r \to 0$ [46].

$$K_{mc} = \sigma_{33}\sqrt{\pi r} \tag{16}$$

Eq. (15) gives the ratio of the crack driving force of a delamination microcrack relative to the Mode I main crack. Crack-divider delamination occurs when the inequality represented by

$$\frac{K_{mc}}{K_I} \geq \frac{K_{IC}^{ST}}{K_{IC}^{LT}} \tag{17}$$

is satisfied for a Mode I crack loaded in the LT orientation. In Eq. (17), K_{IC}^{ST} and K_{IC}^{LT} are the critical stress intensity factors for the short-transverse (ST) and LT orientations, respectively. Combining Eq. (15) and (17) leads one to the following equation for one orientation

$$\frac{K_{IC}^{ST}}{K_{IC}^{LT}} \leq \sqrt{2}\eta\nu \tag{18}$$

which gives the fracture toughness anisotropy required for the onset of crack-divider delamination. For plane strain fracture of an elastically isotropic material where η = 1 and ν = 1/3, the fracture toughness anisotropy required for crack-divider delamination is

$$\frac{K_{IC}^{ST}}{K_{IC}^{LT}} \leq \frac{\sqrt{2}}{3} \tag{19}$$

For the plane stress condition, η = 0 and crack-divider delamination is predicted not to occur unless K_{IC}^{ST} = 0. Thus, crack-divider delamination during plane stress fracture is difficult because of the absence of triaxial stresses induced by plastic constraint.

Once crack-divider delamination has commenced, the stress state in the delamination zone can be obtained from Eq. (15) by setting K_{mc} = K_{IC}^{ST}, leading to

$$\eta = \frac{K_{IC}^{ST}}{\sqrt{2}\nu K_I} \tag{20}$$

which can be combined with Eq. (8) to obtain

$$\frac{K_{IC}^{ST}}{\sqrt{2}\nu K_I} = 1 - \frac{16\left(1-\nu^2\right)}{3\pi}\chi \tag{21}$$

leading to the following expression for χ as a function of K for a Mode I crack

$$\chi = \frac{3\pi}{16\left(1-\nu^2\right)}\left[1-\frac{K_{IC}^{ST}}{\sqrt{2}\nu K_I}\right] \tag{22}$$

The onset of crack-divider delamination commences under the following condition

$$\frac{K_{IC}^{ST}}{K_I} \le \sqrt{2}\nu \tag{23}$$

The condition of Eq. (23) has two important implications: (1) crack-divider delamination microcracks form only in the presence of fracture toughness anisotropy such that $K_{IC}^{ST} \le \sqrt{2}\nu K_I$, and (2) crack-divider delamination occurs before extension of the Mode I crack. The stress state parameter η decreases and the delamination crack density increases with diminishing rates with increasing K_I and χ does not reach the limiting value required to fully relax the constraint stress (η) to zero so that conditions where a true plane stress condition exists are difficult to achieve. This indicates that some level of constraint stress generally exists to continually drive additional cracking as delamination cracking occurs.

Further insight into the evolution of delamination crack density with loading can be obtained by differentiating Eq. (22) with respect to K, leading to

$$\frac{d\chi}{dK} = \frac{3\pi}{16\sqrt{2}\nu(1-\nu^2)}\left[\frac{K_{IC}^{ST}}{K_I^2} - \frac{dK_{IC}^{ST}}{dK_I}\right] \tag{24}$$

which indicates that crack-divider delamination would cease under the condition given by

$$\frac{dK_{IC}^{ST}}{dK_I} = \frac{K_{IC}^{ST}}{K_I^2} \tag{25}$$

leading to the following expression for the change in crack length

$$\frac{1}{K_{IC}^{ST}}\frac{dK_{IC}^{ST}}{da} = \frac{1}{K_I^2}\frac{dK_I}{da} \tag{26}$$

which indicates that the growth of the crack-divider delamination zone also depends on the K-resistance curves for the delamination (ST) and the main crack growth (LT) orientations. The same analysis in Eqs. (13) through (26) would also apply to the TL orientations.

B. *Comparison of Model Prediction and Experimental Data*

Experimental values of the delamination crack density parameter, χ, were determined using Eq. (9) by measuring the maximum diameter ($2r_d$) of the delamination zone from C-scan images at various K levels, metallographic sections from unfractured specimens at the maximum K, and fractographic examinations in some cases. The values of total opening of the delamination microcracks, ($n_c\delta_c$), and therefore the value of $n_c l$ are assumed to remain a constant since the maximum value of the microcracking strain, ε_{mc}, is limited by Eq. (3), and Eq. (9) is simplified to $\chi = r_d / t$ by assuming $n_c = 1$. The increase in delamination zone size with increasing applied K levels for ODS, TZM, and LCAC is shown in Figures 17, 18, and 19, respectively, to produce increases in χ that are lower than the maximum of 0.65 (Eq. (10)). The model developed in the previous section for delamination toughening (Eq. (22)) was used to predict the increase in χ with higher K levels, and a reasonable fit was observed for TZM and LCAC, but a slight under-prediction of χ was generally observed at lower K for ODS and a slight over-prediction of K was generally observed for ODS at high K values. The assumed short transverse toughness values for the model fit were 10 MPa$\sqrt{m}$ for ODS, 7.5-10 MPa$\sqrt{m}$ for TZM and 10-33 MPa$\sqrt{m}$ for LCAC. These were determined based on the applied K at which delaminations were observed in Figures 17-19. The assumed short transverse toughness values for ODS and TZM are within the range of values previously determined in the T-S orientation at room-temperature to 100°C using subsized specimens (11 to 53 MPa$\sqrt{m}$) that were 0.5 mm or 0.25 mm thick [14]. Crack propagation out-of-plane was observed in the T-S orientation for TZM and ODS, and the toughness results are not a valid measurement and are estimates of toughness. Nevertheless, these results indicate that the lower short-transverse toughness for ODS and TZM produces the high tendency for delaminations to be formed that lead to thin sheet toughening. Higher short transverse toughness values are predicted to model the behavior of LCAC (10-33 MPa$\sqrt{m}$) that are also within the range of toughness values determined for LCAC in the T-S orientation at

room-temperature to 200°C (30 to 80 MPa $\sqrt{\mathrm{m}}$), where out-of-plane crack propagation was also observed and the measured toughness values are estimates. The toughness value for LCAC in the short-transverse orientation is higher than ODS and TZM, which likely explains the smaller delamination zone sizes observed for LCAC.

The increase in the χ value prior to the onset of fracture was shown to correlate with higher fracture toughness values for the Mo-alloys at 150°C in Figure 20 (LT TZM was tested at 100°C). The higher delamination crack density and fracture resistance in the ODS molybdenum alloy appears to originate from the fine-grained microstructure, a propensity to grain boundary fracture to divide the material into laminates perpendicular to the fracture surface, and the tendency for the thin laminates to exhibit plasticity. However, LCAC molybdenum exhibited lower fracture toughness values despite a relatively high delamination crack density. One possible explanation for this behavior may be the larger grain size in this microstructure and the propensity of the thin sheet ligament to fail by cleavage fracture due to the larger grain sizes. To better understand the different fracture behaviors observed in these Mo-alloys, the effects of grain size and the role of delaminations were evaluated in terms of the thin-sheet toughening mechanism in the next section.

C. *Thin Sheet Toughening*

The increase in fracture resistance in thin sheet toughening arises from relaxation of the triaxial stresses at the crack tip, an increase in the critical strain to fracture resulting from relaxation of constraint, and enhanced plastic deformation of thin sheet ligaments in the fracture process zone that results from a decrease in constraint. The critical stress intensity factor at fracture is given by the relation [26]

$$K_{IC} = \sqrt{\frac{E\sigma_y n^2 r_o \overline{\varepsilon}_f}{\alpha(1-\nu^2)}} \tag{27}$$

where σ_y is yield stress, E is Young's modulus, α (= 0.65) is a constant relating crack opening displacement to the J-integral, $\bar{\varepsilon}_f$ is the effective strain at fracture, n is the strain hardening exponent, and $n^2 r_o$ gives the size of the process zone ($h = n^2 r_o$) with the assumption of r_o = 0.01 m [26]. The effective strain at fracture is generally on the order of $\varepsilon_{1f}/3$, where ε_{1f} is the fracture strain under uniaxial tension. When thin sheet toughening is operative, the stress state in the process zone evolves from plane strain to plane stress, which increases the fracture strain from $\varepsilon_{1f}/3$ to ε_{1f}. This results in an increase in fracture toughness by a factor of $\sqrt{3}$, providing that the process zone size remains constant. Delamination zone measurements performed in this study reveal two important features for thin sheet toughening in the Mo-based alloys: (1) crack-divider delamination does not completely relax the stress state from the plane strain to the plane stress condition so that the increase in the strain at facture is smaller than $\sqrt{3}$, and (2) crack-divider delamination results in an increase in the length of the process zone beyond the crack tip plastic zone (Table III). Because of the two competing effects, the increase in fracture toughening by thin sheet ligaments is not limited to $\sqrt{3}$, but depends on the delamination zone size. The higher fracture toughness observed in the Mo-based materials showing thin sheet toughening can be attributed to thin sheet toughening with a large delamination zone due to a larger delamination crack density.

Based on the results of the crack-divider delamination analysis, two modifications of Eq. (27) are required to properly describe thin-sheet toughening in Mo-based alloys: (1) a stress state that is between those of the plane strain and the plane stress conditions, and (2) a larger than expected delamination zone size. The term χ is used in the expression given by

$$K_C = \sqrt{\frac{E\sigma_y \bar{\varepsilon}_f n^2 r_o (1 + z\chi)}{3\left(1 - \frac{2}{3} z\chi\right)\alpha\left(1 - \nu^2\right)}} \qquad (28)$$

$$z = \frac{16\left(1-\nu^2\right)}{3\pi} \tag{29}$$

The $(1 + z\chi)$ term was motivated by the direct relation between r_d and χ and the $3(1 – 2z\chi/3)$ term was obtained by combining the stress state parameter η and the reduction of $\bar{\varepsilon}_f$ by the stress state for $\bar{\varepsilon}_f = \varepsilon_{1f}$ at plane stress to $\bar{\varepsilon}_f = \varepsilon_{1f}/3$ at plane strain. The correlation between measured fracture toughness and χ shown in Figure 20 is closest when Eq. (28) is used rather than Eq. (27), and by increasing r_o = 0.01 m to r_o = 0.06 m, which was determined from the experimental plastic zone size measurements. The larger delamination zone size increases the fracture toughness in TZM and LCAC molybdenum. The observed fracture toughness values for ODS exceed those computed on the basis of thin-sheet toughening because additional toughening mechanisms likely result from the aligned grain structure and the formation of these very thin sheets, such as crack branching and crack deflection.

V. DISCUSSION

Examinations of fracture surfaces and crack tip show that the fracture process observed for ODS is different than LCAC and TZM, which can be attributed in part to grain size. ODS exhibits a greater tendency for microcrack formation at grain boundaries with finer ligament sizes that exhibit a high degree of stretching. The cracks in LT-ODS were observed to move out-of-plane. TZM and LCAC exhibit some stretching of ligaments and a tendency for cleavage that likely results from slip band decohesion prior to crack extension. Since TZM and LCAC were only tested at temperatures near the DBTT, while ODS was tested at temperatures above the DBTT (owing to the inherently lower DBTT of ODS), a greater propensity for cleavage would be expected for LCAC and TZM. A greater fraction of ductile laminate features are observed for TZM and LCAC at higher test temperatures above the DBTT, but TZM and LCAC are observed to exhibit a greater fraction of cleavage at the fracture surface than observed for ODS at all test temperatures [14-16]. Fracture toughness values ranging from 5 to 10 MPa $\sqrt{\text{m}}$ have been

reported in literature for cases where predominant grain boundary fracture is observed in molybdenum [9,47]. Studies of molybdenum bi-crystals have shown that molybdenum has weak boundaries where the fracture stress values are low, and the toughness values could be considered to be about 1 MPa $\sqrt{m}$ for cases where the grain boundaries are contaminated with oxygen [10-13]. This is significantly lower than the toughness values determined for the T-S orientation in this work. Taken together, these observations indicate that weak grain boundaries are likely absent, or present in only very small amounts, in the Mo-base alloys studied herein. Thus, crack-divider delamination does not necessarily imply that the grain boundaries are weak or exhibit low fracture resistance. However, the propagation of microcracks in an orientation where delamination occurs along grain boundaries that are perpendicular to the crack plane produces the crack-divider delamination toughening observed for the wrought molybdenum alloys in this work. This indicates the toughness for these wrought molybdenum-base materials is inherently anisotropic.

The model developed in this investigation clearly shows that crack-divider delamination originates from anisotropy in fracture toughness but is microstructurally introduced. In particular, crack-divider delamination is predicted to occur when the short-traverse fracture toughness value is less than about 47% of those for the LT or TL orientation. The model also predicts that crack-divider delamination would occur before the growth of the main crack. Both of these predictions were confirmed by ultrasonic C-scan measurements, which showed crack-divider delamination did occur at a K level less than 1/2 of the plane strain fracture toughness. The ultrasonic C-scan and the subsequent metallographic characterization of the sectioned specimens also confirmed the presence of thin-sheet toughening in the ODS, TZM, and LCAC molybdenum at temperatures $\leq$ 150°C. Comparison of the experimental data and model prediction revealed that the relaxation of triaxial stresses in the process zone does not always reach the plane stress condition and the size of the crack-divider delamination zone is much

larger than the crack tip plastic zone. The consequence is that the observed thin sheet toughening is larger than the theoretical factor of $\sqrt{3}$.

The pancake-shaped grain structure appears to be responsible for the fracture toughness anisotropy observed in these wrought Mo-based alloys. Since the various grain boundary dislocation mechanisms show a Hall-Petch type dependence for yield strength or toughness on grain-size, a pancake-shaped grain morphology would allow easy dislocation creation and motion in the direction with a larger mean-free path for dislocation motion, but dislocation creation and motion would be more difficult in the direction with a shorter mean-free path. As a result, a lower fracture resistance is produced in the hard slip direction (i.e, the ST orientation) where the mean free path between the laminates is short and stresses may build up more rapidly to produce cracking at grain boundaries. A higher fracture resistance prevails in the easy slip direction (LT or TL) where distance between boundaries is long so that dislocation motion prevents a large build-up of stresses at grain boundaries. This anisotropy in deformation of the pancake-shaped grain microstructure of these wrought molybdenum alloys results in the nucleation of delamination cracks along grain boundaries in the ST orientation that produce the thin sheet toughening mechanism.

The fracture mechanism in the thin sheet ligaments plays an important role in determining the observed fracture toughness value. Ductile ligaments are observed at the fracture surface of ODS, TZM, and LCAC molybdenum, which indicate that thin sheet toughening is important. However, ODS has the finest grain size and lowest fraction of cleavage features are observed at the fracture surface, while LCAC has the largest fraction of cleavage features and the largest grain size. TZM represents an intermediate case. The fracture process for ODS appears to occur by uniform microcracking along boundaries to produce very fine thin-sheet ligaments that exhibit a high propensity for ductile behavior under plane stress conditions. Microcrack formation was not observed for TZM and LCAC and both exhibited a tendency for cleavage fracture of the thin sheet ligaments produced by crack-divider

delamination. The cleavage facets were relatively large and probably originated from larger grains in the microstructure. Since the cleavage facets were generally inclined to the stress axis when viewed in stereo-pairs, they are likely formed by decohesion of planar slipbands. Planar slipbands and sliplines were observed at the crack tips of LCAC molybdenum at high K levels, but were not observed for TZM. TZM was observed to form an extensive delamination zone at the crack tip that was similar to that observed for ODS. This suggests TZM is an intermediate case to ODS and LCAC, but the finer grain size for ODS results in a greater tendency for microcracking along boundaries at the crack tip with a high fraction of ligament ductility while a larger grain size results in a tendency for slipband formation at the crack tip that leads to cleavage with a less extensive delamination zone and lower fraction of ligaments that exhibit ductile behavior. The finer grain size (about 1-2 μm thickness of sheet-like grains) might have suppressed cleavage in ODS molybdenum, while the larger grain size (4-15 μm thickness of sheet-like grains) in the TZM and LCAC molybdenum might have made these alloys more prone to cleavage fracture. The cleavage mode observed for LCAC and TZM molybdenum appears to result in a lower fracture toughness and higher DBTT compared to the fracture mode observed for ODS, which starts by microcracking along grain boundaries.

VI. CONCLUSIONS

1. In-situ testing, ultrasonic C-scans, metallography, and fractography were used to show that a crack-divider delamination form of thin-sheet toughening occurred in wrought ODS, TZM, and LCAC molybdenum at temperatures near their respective DBTTs. Cracking along boundaries leaves ligaments that may stretch plastically to produce the observed toughening.
2. Fracture toughness anisotropy with a lower fracture toughness in the short-transverse direction produces the crack-divider delamination in fracture specimens tested in the LT and TL orientations. Crack-divider delamination occurred in Mo-based alloys at a

K level governed by the fracture toughness of the short-transverse orientation and before the growth of the main crack in the LT or TL orientation.

3. The diameter of the crack-divider delamination zone in the Mo-based alloys increases with increasing K and is larger than the corresponding plastic zone diameter. A larger-than expected process zone is created by extensive crack-divider delamination that leads to substantial thin-sheet toughening in Mo-based alloys. Additional toughening by crack deflection along grain boundaries is also present in ODS molybdenum in the LT orientation. Theoretical prediction of the evolution of delamination crack density with stress intensity factor is in agreement with experimental data obtained by ultrasonic C-scans, metallography, and fractography.
4. The fracture mechanism, cleavage or grain boundary fracture that produces plane stress conditions allowing extensive plasticity for thin sheet ligaments, in the thin-sheet ligaments appears to dictate the observed fracture toughness with lower fracture toughness values for cleavage in the thin-sheet ligaments. Fracture in ODS Mo-alloys proceeds mainly along grain boundaries to produce small ligaments that exhibit ductility for both LT and TL orientations, while a combination of grain boundary fracture and cleavage is prevalent in LCAC molybdenum and TZM. The predominance for microcracking along grain boundaries to leave fine ligaments in ODS molybdenum can be attributed to a fine-grained microstructure with ≈1-2 μm thickness of sheet-like grains. The presence of mixed grain boundary fracture and cleavage in LCAC molybdenum and TZM can be attributed to a microstructure with a larger thickness of sheet-like grains (4 - 15 μm).

VII. ACKNOWLEDGEMENTS

This work was supported under USDOE Contract No. DE-AC11-98PN38206. The advice and review of W.J. Mills, R.W. Smith, and J.E. Hack are much appreciated.

REFERENCES

1. J.B. Lambert and J.J. Rausch: *Non-Ferrous Alloys and Special-Purpose Materials, Materials Handbook, Vol. 2,* ASM International, Materials Park, OH, 1992, pp. 557-582.
2. R.E. Gold, and D.L. Harrod: *J. of Nuclear Materials*, 1979, vol. 85-85, pp. 805-815.
3. B.L. Cox, and F.W. Wiffen: *J. of Nuclear Materials*, 1979, vol. 85-85, pp. 901-905.
4. G.R. Smolik, et. al: *J. of Nuclear Materials*, 2000, vol. 283-287, pp. 1458-1462.
5. J. Wadsworth, T. G. Nieh, and J. J. Stephens: *Int. Materials Reviews*, 1988, Vol. 33, No. 3, pp. 131-150.
6. R. N. Orava: In Refractory Metals and Alloys IV – Research and Development, edited by K. I Jaffee, G. M. Ault, J. Maltz, and M. Semchyshen, Gordon and Breach, NY, 1967, pp. 117-140.
7. B. A. Wilcox and A. Gibert: In Refractory Metals and Alloys IV – Research and Development, edited by K. I Jaffee, G. M. Ault, J. Maltz, and M. Semchyshen, Gordon and Breach, NY, 1967, pp. 95-115.
8. A. Lawley: In Refractory Metals and Alloys IV– Research and Development, edited by K. I Jaffee, G. M. Ault, J. Maltz, and M. Semchyshen, Gordon and Breach, NY, 1967, pp. 141-160.
9. B. S. Lemet and K. Kreder: In Refractory Metals and Alloys IV – Research and Development, edited by K. I Jaffee, G. M. Ault, J. Maltz, and M. Semchyshen, Gordon and Breach, NY, 1967, pp. 161-183.
10. H. Kurishta, A. Oishi, H. Kubo, and H. Yoshinaga: *Trans. J. Inst. Metals,* 1985, Vol. 26, No. 5, pp. 341 – 352.
11. H. Kurishita and H. Yoshinaga: *Materials Forum*, 1989, vol. 13, pp. 161-173.
12. S. Tsurelawa, T. Tanaka, and H. Yoshinaga: *Mat. Sci. and Eng.,* 1994, Vol. A176, pp. 341– 348.
13. A. Kumar and B.L. Eyre: *Proc. R. Soc. Lond.*, 1980, vol. A370, pp. 431-458.

14. B. V. Cockeram: *Met. Trans.*, 2002, Vol. 33A, pp. 3685-3707.

15. B. V. Cockeram: *Met. Trans.*, 2005, Vol. 36A, pp. 1777–1791.

16. B. V. Cockeram: *Mat Sci. Eng A*, 2006, Vol. 418, pp. 120–136.

17. C. Grandhi and M.F. Ashby: *Acta Met.*, 1979, vol. 27, pp. 1565-1602.

18. M. Semchyshen and R.Q. Barr: *J. Less-Common Metals*, 1966, vol. 11, pp. 1-13.

19. J.C. Thornley and A.S. Wronski: *Acta Met.*, 1970, vol. 18, pp. 1053-1062.

20. A.A. Johnson,S.P. Gupta, and S.P. Kodali: *Mat. Sci. & Eng*, 1975, vol. 18, pp. 159-161.

21. S. Morozumi, : *Proc. Mechanical Properties of bcc Metals,* Metallurgical Society/AIME, 1982, pp. 197-205.

22. A. Lawley, J. Van den Sype, and R. Maddin, *J of the Institute of Metals*, 1962-1963, vol. 91, pp. 23-27.

23. G.W. Brock: *Trans. Met. Soc. AIME*, 1961, vol. 221, pp. 1055-1062.

24. W.D. Klopp: *J. Less Common Met.,* 1975, vol. 42 pp. 261-278.

25. J. Wadsworth, T.G. Nieh, and J.J. Stephens: *Scripta Met.*, 1986, vol. 20, pp. 637-642.

26. K. S. Chan: *Met. Trans.*, 1989, Vol. 20A, pp. 155-164.

27. K. S. Chan: *Met. Trans.*, 1989, Vol. 20A, pp. 2337-2344.

28. J. D. Embury, N. J. Petch, A. E. Wraith, and E. S. Wright: *Trans. AIME,* Vol. 239, pp. 114-118.

29. K. T. Venkateswara Rao, W. Yu, and R. O. Ritchie: *Metall. Trans. A.,* A988, Vol. 19A, pp. 549-561.

30. S. Yokoshima and M. Yamaguchi: *Acta Metal.,* 1996, Vol. 44, No. 3, pp. 873-883.

31. R. R. Adharapurapu, K. S. Vecchio, A. Rohatgi, and F. Jiang: Metall. *Mater. Trans. A.,* 2005, Vol. 36A, pp. 3217-3236.

32. *Standard Specification for Molybdenum and Molybdenum Alloy Plate, Sheet, Strip, and Foil*, ASTM B386-91, American Society for Testing and Materials, Philadelphia, PA, 1997.

33. R. Bianco, R.W. Buckman, Jr., and C.B. Geller: *High Strength, Creep-Resistant Molybdenum Alloy and Process For Producing the Same*, US Patent #5,868,876, February 9, 1999.

34. A.J. Mueller, J.A. Shields, and R.W. Buckman, Jr.*: Proc. 15th Int. Plansee Seminar, Vol. 1*, G. Kneringer, P. Rodhammer and H. Wildner, Eds., Plansee Holding AG, Reutte, Austria, 2001, pp. 485-497.

35. K. S. Chan: *Met. Trans.*, 1996, Vol. 27A, pp. 2518-2531.

36. *Standard Terminology Relating to Fatigue and Fracture Testing*, ASTM E1823-96, American Society for Testing and Materials, Philadelphia, PA, 1996.

37. ASTM E812-97, ASTM, Philadelphia, PA, 1997.

38. ASTM E813-95, ASTM, Philadelphia, PA, 1995.

39. T. G. F. Gray: *Int. Journal of Fracture,* 1977, Vol. 13, No. 1, pp. 65-75.

40. A. Nagy, J. B. Campbell, and D. L. Davidson: *Rev. Sci. Instrum.,* 1984, Vol. 55, pp. 778-782.

41. *Standard Test Method for Plane-Strain Fracture Toughness of Metallic Materials*, ASTM E399-90, American Society for Testing and Materials, Philadelphia, PA, 1997.

42. D. R. Williams, D. L. Davidson, and J. Lankford, *Exp. Mech.,* 1980, Vol. 20, pp. 134-139.

43. E. A. Franke, D. J. Wenzel, and D. L. Davidson: *Rev. Sci. Instrum.,* 1990, Vol. 62(5), pp. 1270-1279.

44. *Standard Test Method for Measurement of Fracture Toughness*, ASTM E1820-01, American Society for Testing and Materials, Philadelphia, PA, 2001.

45. X. Q. Feng and D. Gross: *Int J. Damage Mech.,* 2000, Vol. 9, pp. 79-112.

46. M.-Y. He and J. W. Hutchinson: *Int J. Solids and Structure,* 1989, Vol. 25, No. 9, pp. 1053-1067.

47. Z. Jiuxing, L. Lu, Z. Meiling, H. Yancao, and Z. Tieyong: I*nt. J. Refractory Metals & Hard Materials,* 1999, Vol. 17, pp. 405-409.

Table I. Summary of previously reported data for LCAC, TZM, and ODS molybdenum alloys [14-16] giving the of chemical analysis, as provided in material certification reports (weight percent ppm), grain size, DBTT values determined from fracture toughness testing, and range of toughness values at temperatures above the DBTT.

Material / Lot#	**C**	**O**	**N**	**Ti**	**Zr**	**Fe**	**Ni**	**Si**	**La**	**Al**	**Ca**	**Cr**	**Cu**	**Other**
ODS Molybdenum / Ingot #382 Heat# LA22963	10	NA	NA	<10	NA	74	12	24	1.6 wt%	21	320	24	10	<10 Mg <10 Mn <10 Pb <10 Sn
TZM Molybdenum / Ingot 61722B Lot# TZM24080	223	17	9	5000	1140	<10	<10	<10	NA	NA	NA	NA	NA	NA
LCAC Molybdenum / Ingot 50823 Lot# C24728	50	11	4	NA	NA	<10	<10	<10	NA	NA	NA	NA	NA	NA
Alloy – Orientation	Grain Width [µm]		Grain Length [µm]			Toughness DBTT			Toughness Values at					
	Average ± Standard Deviation		Average ± Standard Deviation						T ≥ DBTT [MPa √m]					
LCAC Plate – LSR	14.0 ± 10.4		340 ± 138			150°C			45 to 166					
LCAC Plate – TSR	15.2 ± 10.5		255 ± 113			200°C			56 to 175					
TZM Plate – LSR	3.9 ± 2.5		273 ± 105			100°C			49 to 215					
TZM Plate – TSR	6.1 ± 3.8		132 ± 69			150°C			32 to 156					
ODS Plate – LSR	1.4 ± 0.7		29.0 ± 16.2			< -150°C			68 to 205					
ODS Plate – TSR	2.0 ± 1.1		13.6 ± 6.6			25°C			53 to 139					

Note:

1. The compositions for LCAC and TZM are within the ASTM B386-91 specification for these alloys. ASTM B386 – 365 for arc-cast LCAC molybdenum and ASTM B386 – 363 for TZM molybdenum [32].
2. NA = Not available.
3. All material was obtained from H.C. Starck, Cleveland, OH.
4. All of the wrought alloys consist of sheet-like, pancaked grains that are aligned in the longitudinal orientation.
5. The fracture toughness values at temperatures < DBTT ranged from 5.8 to 29.6 MPa√m for ODS, TZM, and LCAC [14-16].

Table II. Summary of Specimens Tested, K Levels for In-Situ Fracture Testing and Ultrasonic C-Scan Measurements, Specimen Condition After Testing, and Fracture Toughness value Measured from In-Situ Fracture Testing

Alloy	Orientation	T,°C	Applied K during testing, MPa $\sqrt{m}$	K Level for C-Scan, MPa $\sqrt{m}$	Specimen Condition After Testing	Measured K_C, MPa $\sqrt{m}$
ODS Mo	L-T	25	5, 10, 15, 18, 20, 22, 24, 26, 28, 30, 32, 34, 36, 38, 40	40	Intact	>40
ODS Mo	L-T	25	10, 15, 20, 25, 30, 35, 40, 45, 50	13^{+}, 15, 25, 35, 50	Intact	>50
ODS Mo	T-L	25	5, 10, 15, 18, 19, 20, 21, 22, 23, 24, 26, 28, 30, 32	32	Intact	>32
ODS Mo	T-L	25	10, 15, 20, 25, 30, 35, 40, 45, 50	13^{+}, 15, 25, 35, 50	Intact	>50
ODS Mo	L-T	150	10, 15, 20, 25, 30, 35, 40, 45, 50, 55, 60, 65	13^{+}, 25, 35, 50, 65	Intact	>65
ODS Mo	T-L	150	10, 15, 20, 25, 30, 35, 40, 45, 50, 50.2	13^{+}, 25, 35, 50, 50.2	Intact	50.2
TZM	L-T	100	10, 15, 20, 25, 30	13^{+}, 25	Fractured	30
TZM	T-L	150	10, 15, 20, 25, 30, 35, 40	13^{+}, 25, 35	Fractured	40
LCAC Mo	L-T	150	10, 15, 20, 25, 30, 35, 40, 42	13^{+}, 25, 35	Fractured	42
LCAC Mo	T-L	150	10, 15, 20, 25, 27.8	13^{+}, 25	Fractured	27.8
LCAC Mo	L-T	200	10, 15, 20, 25, 30, 35, 40, 45, 50, 55, 60, 65, 70	13^{+}, 15, 25, 35, 50, 70	Intact	> 70
LCAC Mo	T-L	200	10, 15, 20, 25, 30, 35, 40, 45, 50, 55, 60, 65, 69	13^{+}, 15, 25, 35, 50	Fractured	69.2

Notes:

1. Tensile K induced during compression/compression fatigue precracking, C-scan performed after fatigue precracking
2. All “Intact” specimens were subjected to sectioning followed by optical metallography.
3. All “Fractured” specimens were subjected to SEM fractography.

Table III. Summary of the Measured Plastic Zone Size, Computed Process Zone Size, Delamination Zone Size, and the Delamination Crack Density Prior to the Onset of Fracture or at the Highest K Level Tested.

Alloy	**Orientation**	**Test Temperature**	**Measured Plastic Zone Size (μm)**	**Process Zone Size (h) (μm)**	**Delamination Zone Size (r_d) (μm)**	**Delamination Crack Density (χ)**
ODS	LT	25°C	150	164.6	1150	0.2722
ODS	TL	25°C	120	113.5	1500	0.3466
ODS	LT	150°C	800-1000	113.5	1560	0.3613
ODS	TL	150°C	100	104.6	1340	0.2810
TZM	LT	100°C	100	106.9	1440	0.3032
TZM	TL	150°C	90	113.9	1710	0.3620
LCAC	LT	150°C	125	180	1000	0.2134
LCAC	TL	150°C	100	79.1	800	0.0375

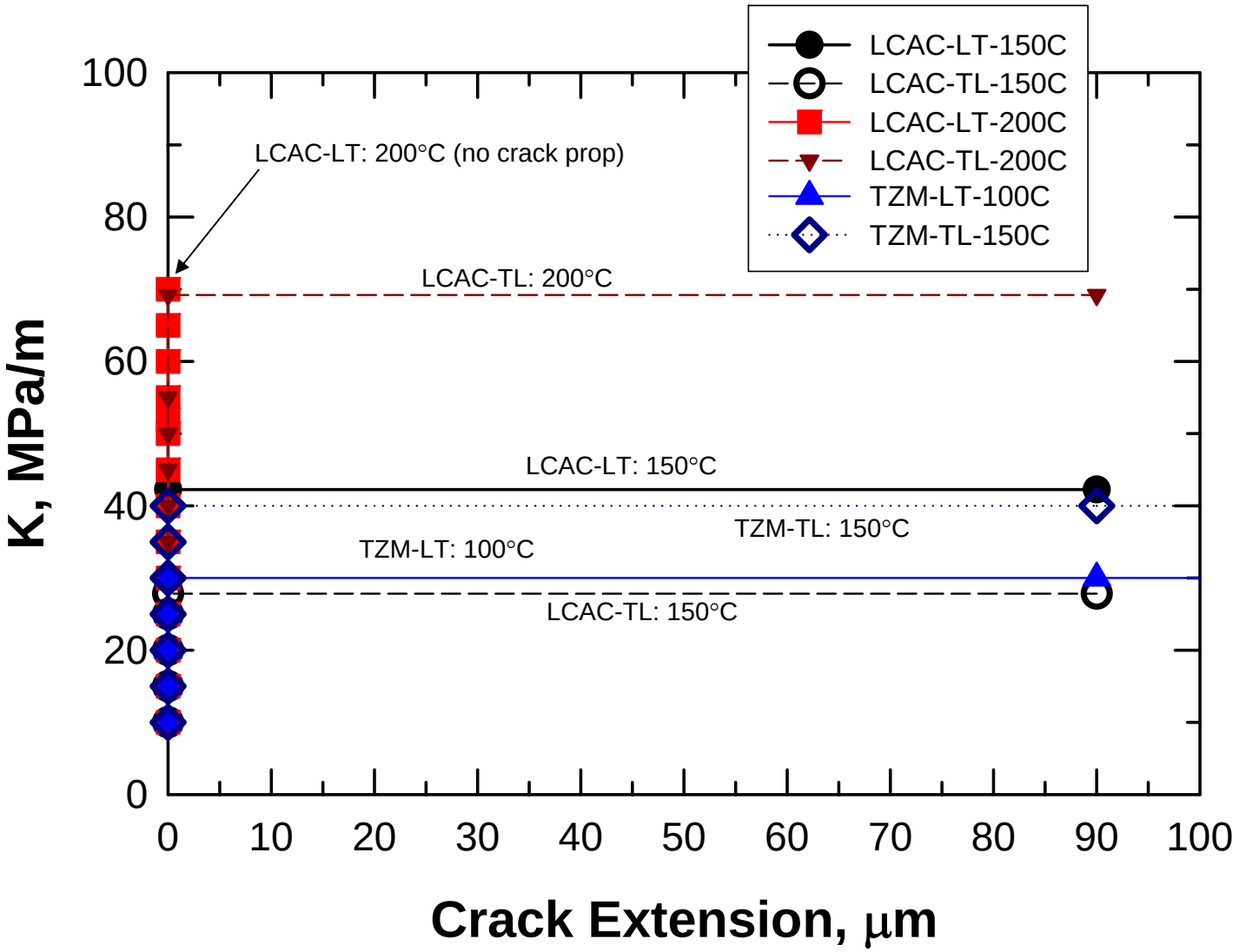

Figure 1. The K-resistance curves determined for LCAC and TZM molybdenum during in-situ toughness testing in a SEM at 100°C to 200°C. Results for these six tests are presented with a summary of data provided in Table 2.

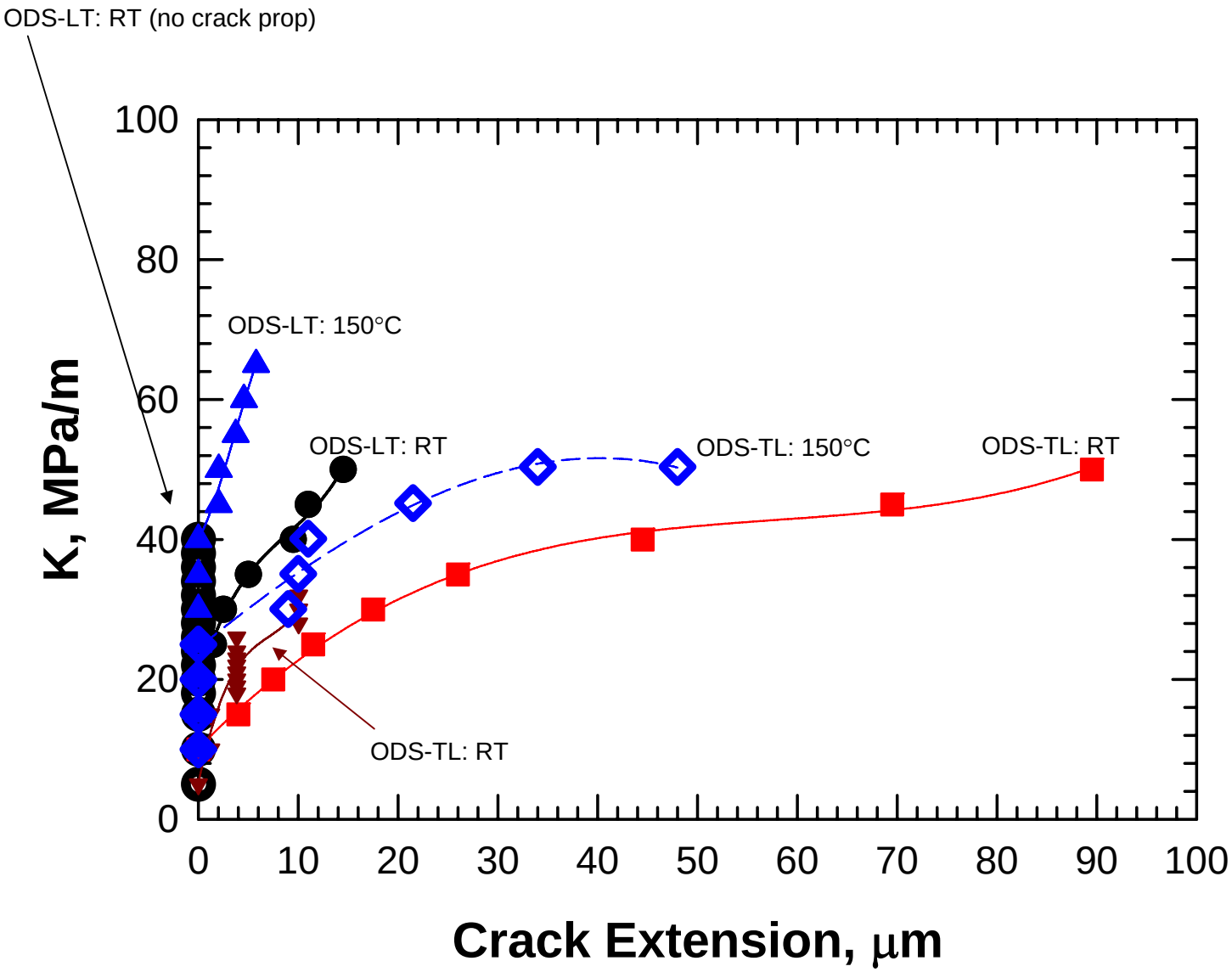

Figure 2. The K-resistance curves determined for ODS molybdenum during in-situ toughness testing in a SEM at room-temperature (RT) and 150°C. Two sets of specimens were tested at RT for both LT and TL ODS. The results from a total of six tests are presented with a summary of data given in Table 2.

(a)

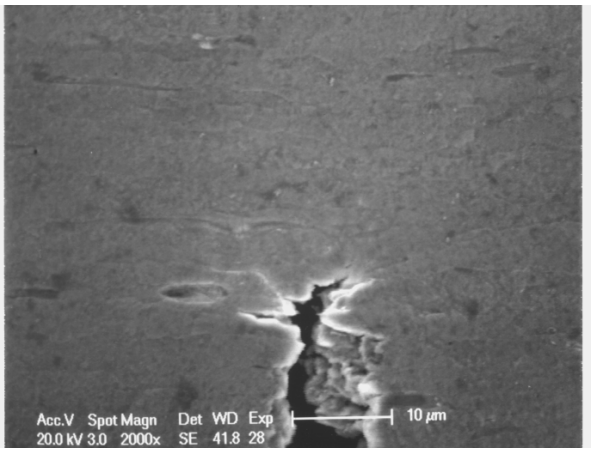

(b)

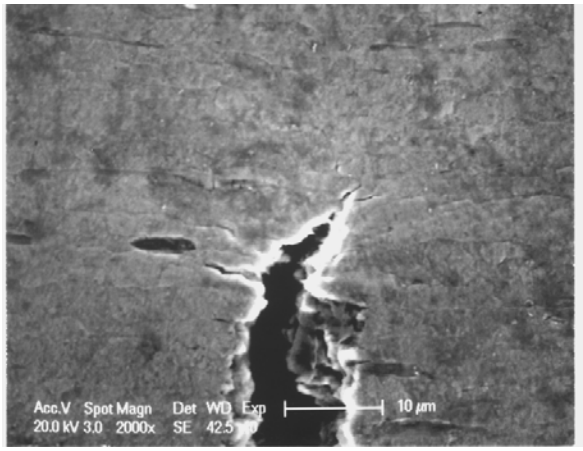

(c)

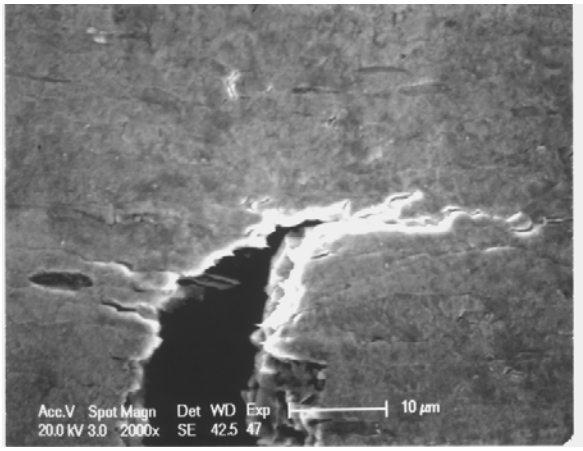

(d)

Figure 3. **SEM micrographs of the crack tip fracture process in ODS molybdenum in the LT orientation tested at room-temperature showing crack branching and deflection along grain boundaries: (a) K = 25 MPa$\sqrt{m}$, (b) K = 35 MPa$\sqrt{m}$, (c) K = 45 MPa$\sqrt{m}$, and (d) K = 50 MPa$\sqrt{m}$. Loading direction is horizontal. Rolling direction is horizontal.**

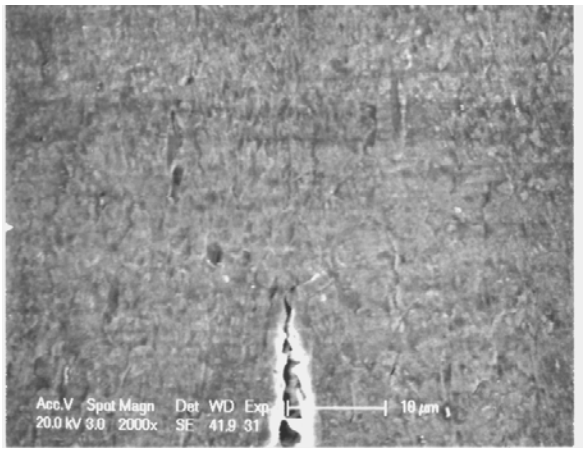

(a)

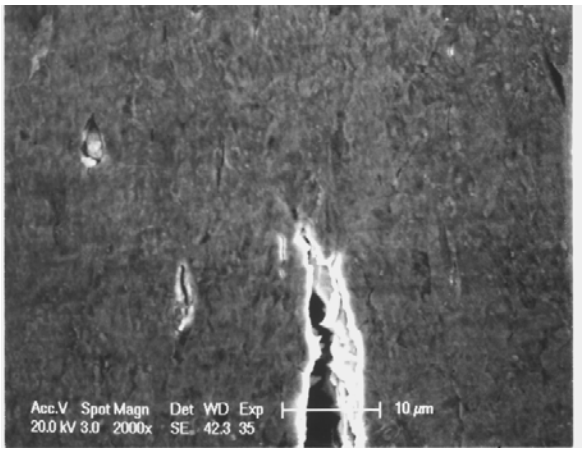

(b)

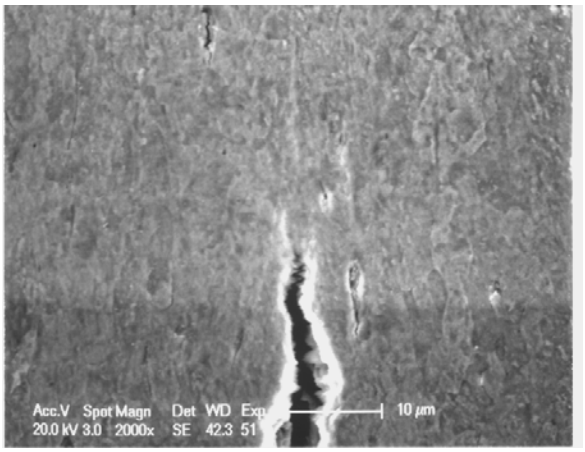

(c)

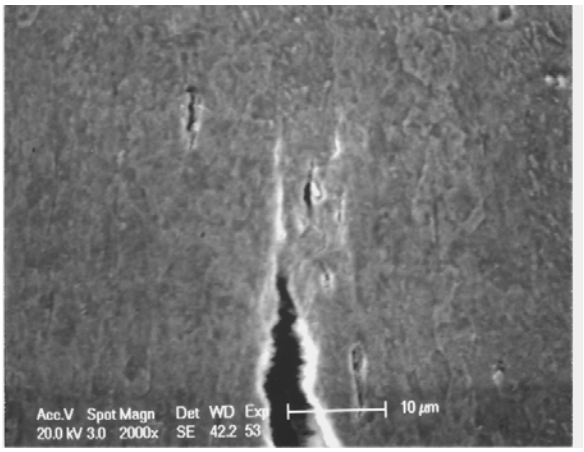

(d)

Figure 4. **SEM micrographs of the crack extension processes in TL ODS molybdenum tested at 25°C: (a) K = 25 MPa $\sqrt{m}$, (b) K = 35 MPa $\sqrt{m}$, (c) K = 45 MPa $\sqrt{m}$, and (d) K = 50 MPa $\sqrt{m}$. Microcracks are observed to be formed at grain boundaries ahead of the crack tip at K ≥ 35 MPa $\sqrt{m}$. The loading direction is horizontal. Rolling direction is vertical.**

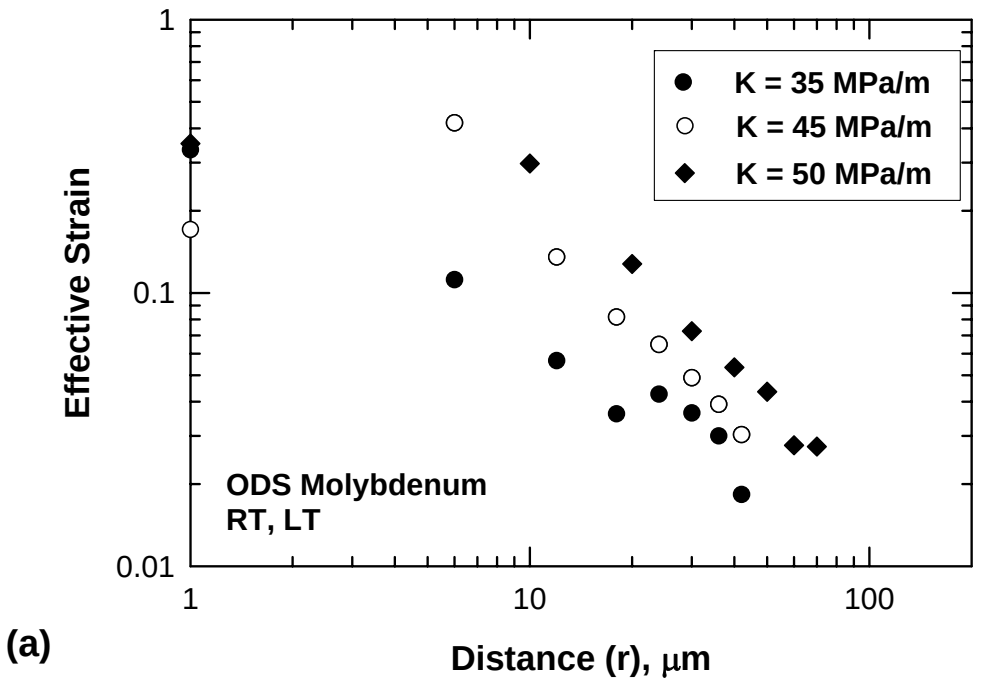

(a)

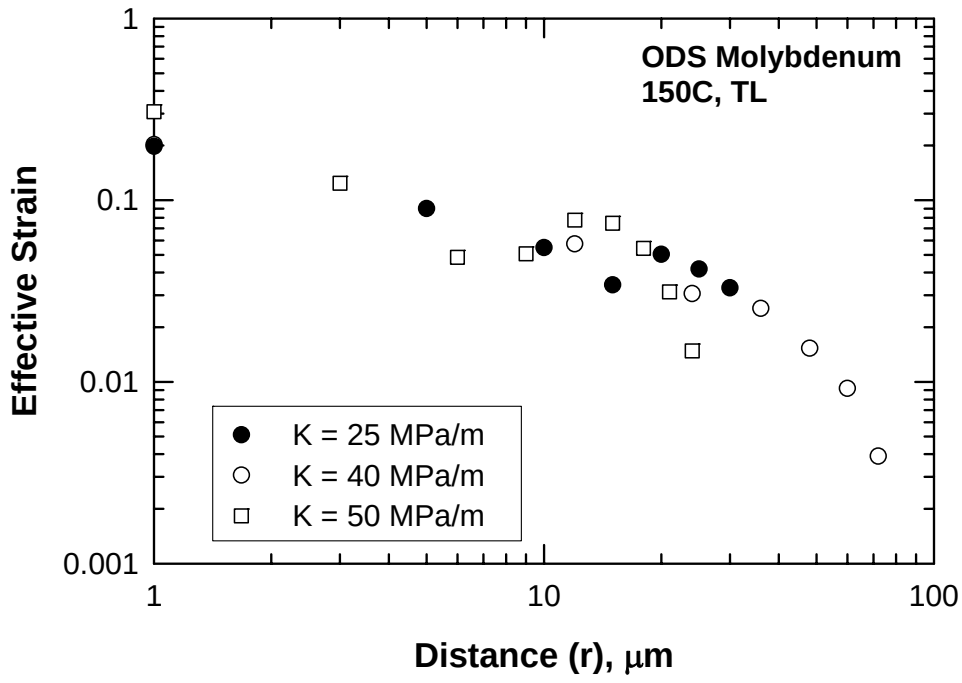

(b)

Figure 5. Near-tip strain distributions for ODS molybdenum: (a) LT orientation tested at room-temperature, and (b) TL orientation tested at 150°C.

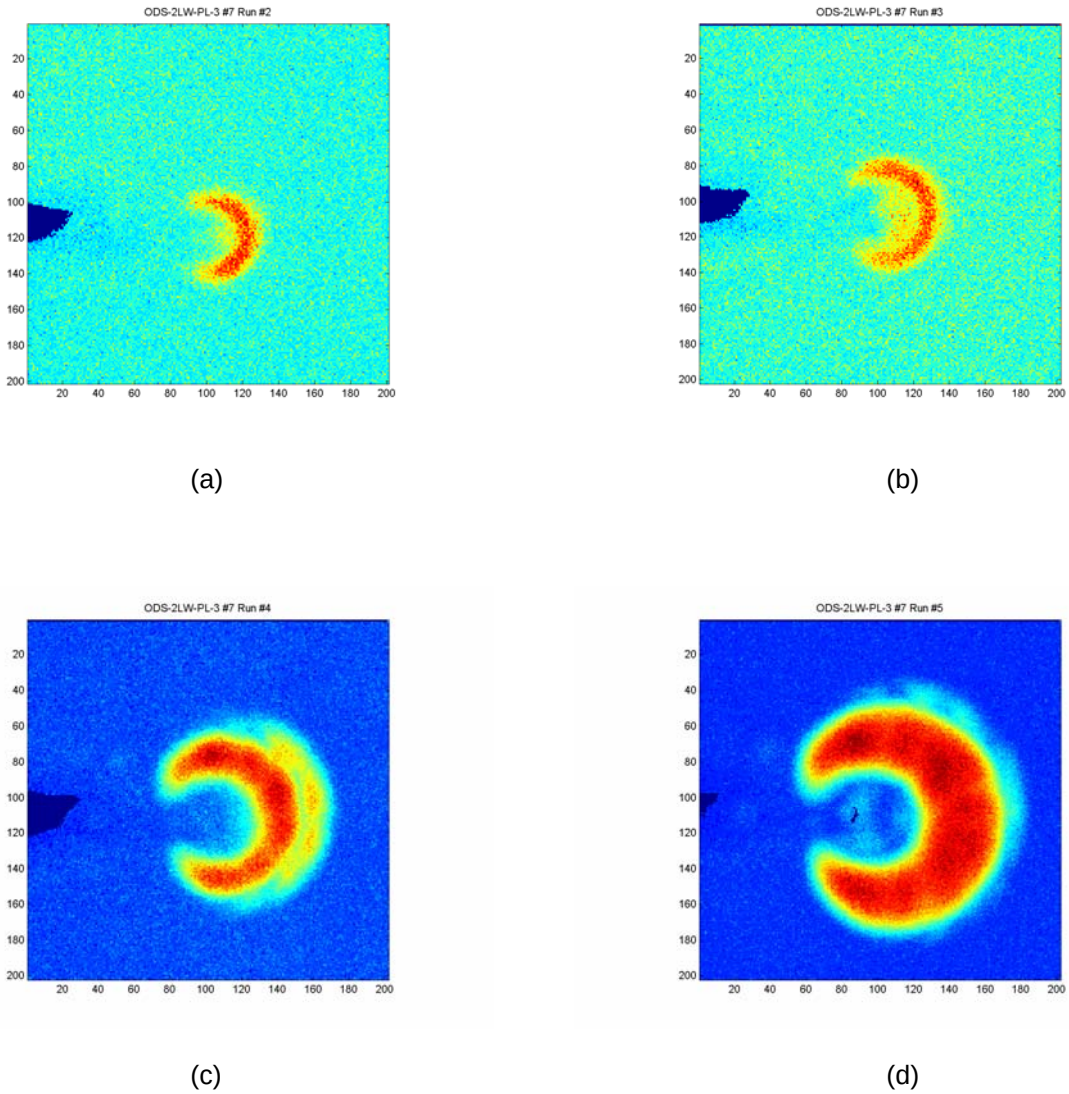

(a) (b)

(c) (d)

Figure 6. **Ultrasonic scan images of the crack tip for LT-ODS molybdenum tested at 150°C showing the presence of internal delamination: (a) K = 25 MPa $\sqrt{m}$, (b) K = 35 MPa $\sqrt{m}$, (c) K = 50 MPa $\sqrt{m}$, and (d) K = 65 MPa $\sqrt{m}$. Blue represents the intact region, while crack separation is highest in the red region, followed by yellow, and then light blue.**

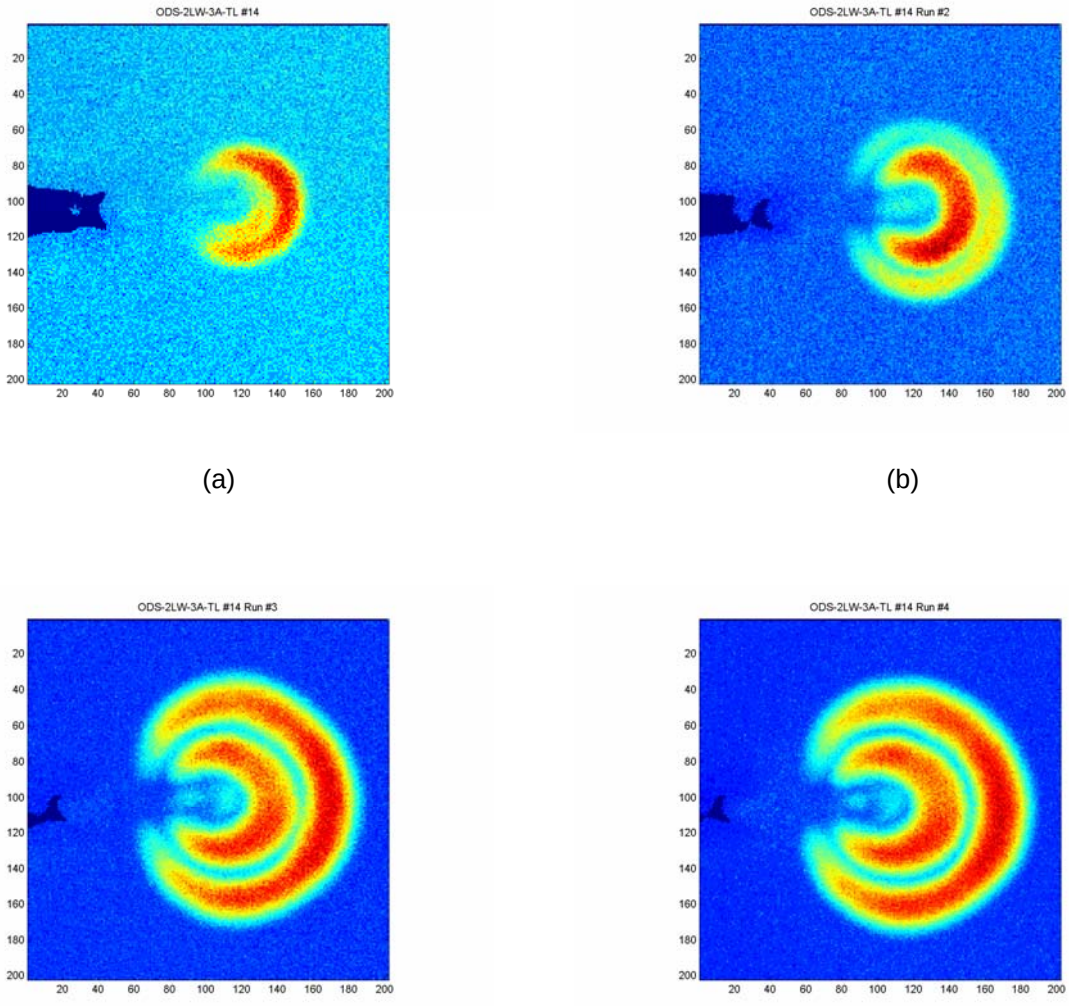

(a) (b)

(c) (d)

Figure 7. **Ultrasonic scan images showing the internal delamination zone in TL-ODS molybdenum tested at 150°C: (a) K = 25 MPa $\sqrt{m}$, (b) K = 35 MPa $\sqrt{m}$, (c) K = 50 MPa $\sqrt{m}$, and (d) K = 50.2 MPa $\sqrt{m}$. Blue represents the intact region, while crack separation is highest in the red region, followed by yellow, and then light blue.**

(a)

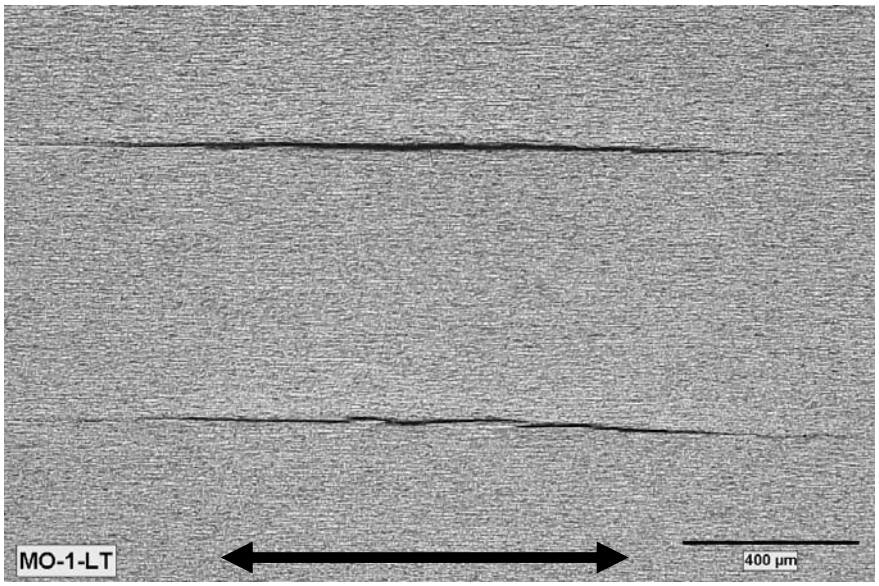

(b)

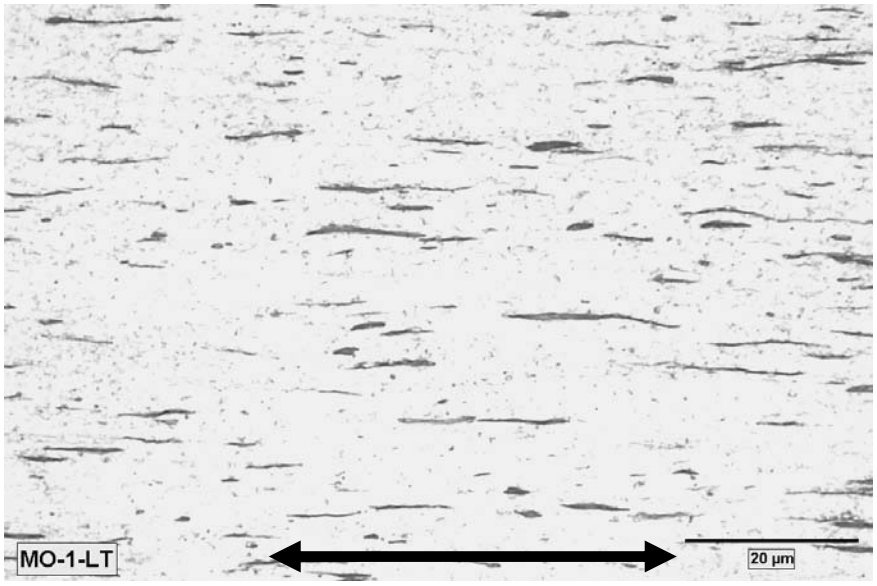

Figure 8. Metallographic sections of the delamination zones at the crack tip for ODS molybdenum specimens that were intact (not-fractured) after testing: (a) LT-ODS tested at room-temperature showing macroscopic delamination cracks, (b) LT-ODS tested at room-temperature showing microscopic delamination cracks in the thin-sheet ligaments between the macroscopic delamination cracks, (c) TL-ODS tested at room-temperature showing cracks from macroscopic delamination, (d) testing of TL-ODS at room-temperature showing microscopic delamination cracks indicated by arrows in the thin-sheet ligaments between the macroscopic delamination cracks, and (e) fracture surface of TL-ODS fractured during pre-cracking. The images for Fig. 8a, 8b, 8c, and 8d were taken from the plane perpendicular to the crack plane in the process zone ahead of the crack tip (Figure 16b) with the arrow shown above parallel to the rolling direction. The surface of the crack plane is shown in Fig 8e that is perpendicular to the rolling direction.

(c)

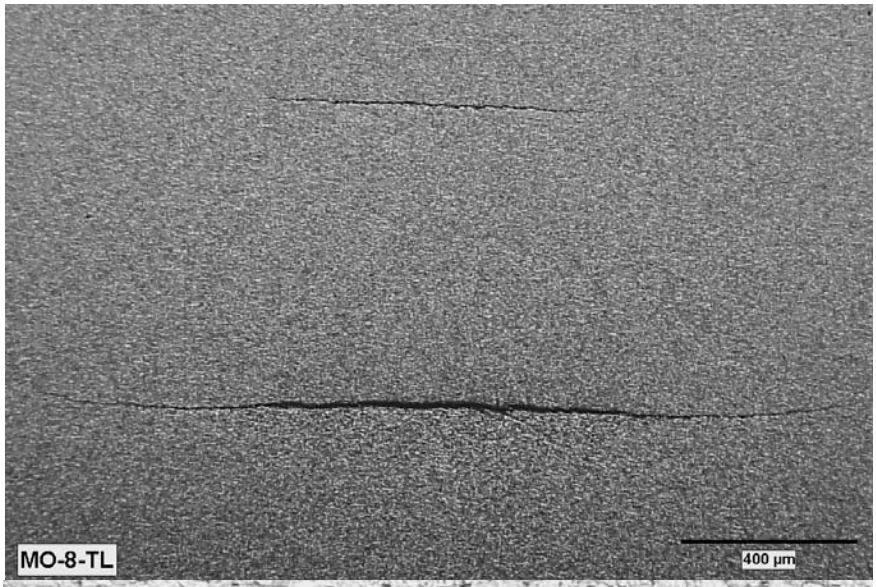

(d)

(e)

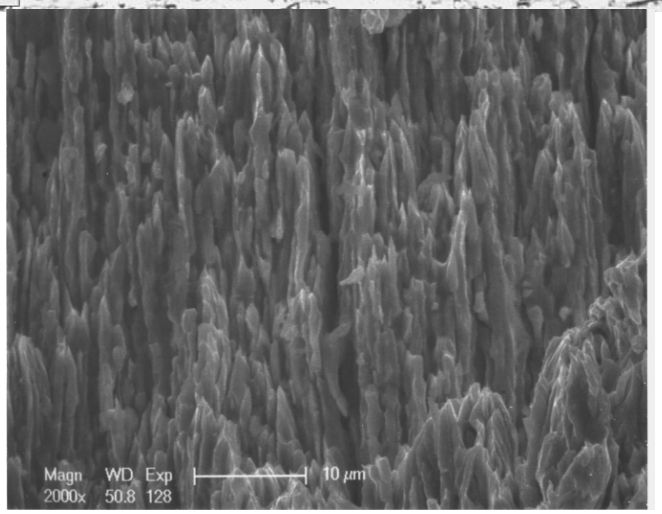

Figure 8. (continued) Metallographic sections of the delamination zones at the crack tip for ODS molybdenum specimens that were intact (not-fracture) after testing: (a) LT ODS tested at room-temperature showing macroscopic delamination cracks, (b) LT ODS tested at room-temperature showing microscopic delamination cracks in the thin-sheet ligaments between the macroscopic delamination cracks, (c) TL ODS tested at room-temperature showing cracks from macroscopic delamination, (d) testing of TL ODS at room-temperature showing microscopic delamination cracks indicated by arrows in the thin-sheet ligaments between the macroscopic delamination cracks, and (e) fracture surface of TL ODS fractured during pre-cracking. The images for Fig. 8a, 8b, 8c, and 8d were taken from the plane perpendicular to the crack plane in the process zone ahead of the crack tip (Figure 16b) with the arrow shown above parallel to the rolling direction. The surface of the crack plane is shown in Fig 8e that is perpendicular to the rolling direction.

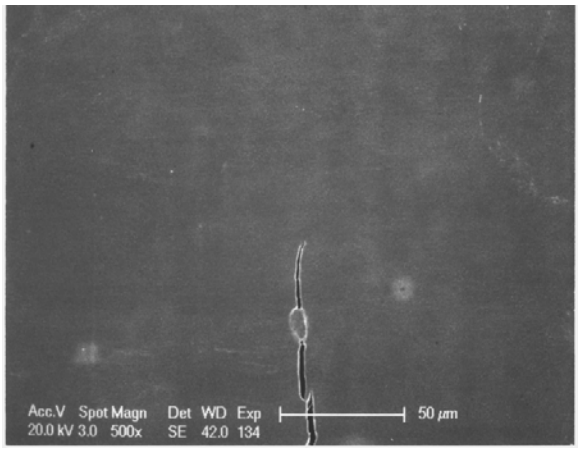

(a)

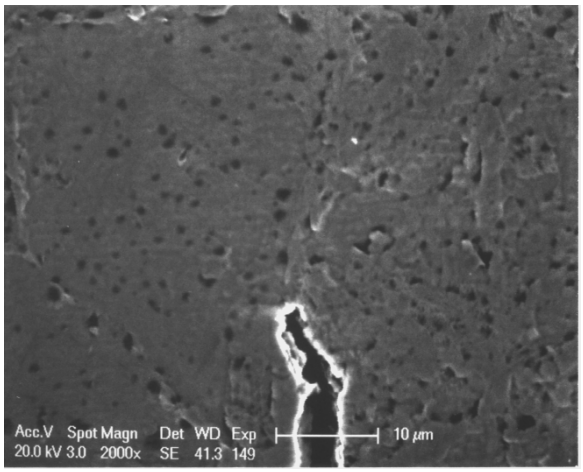

(b)

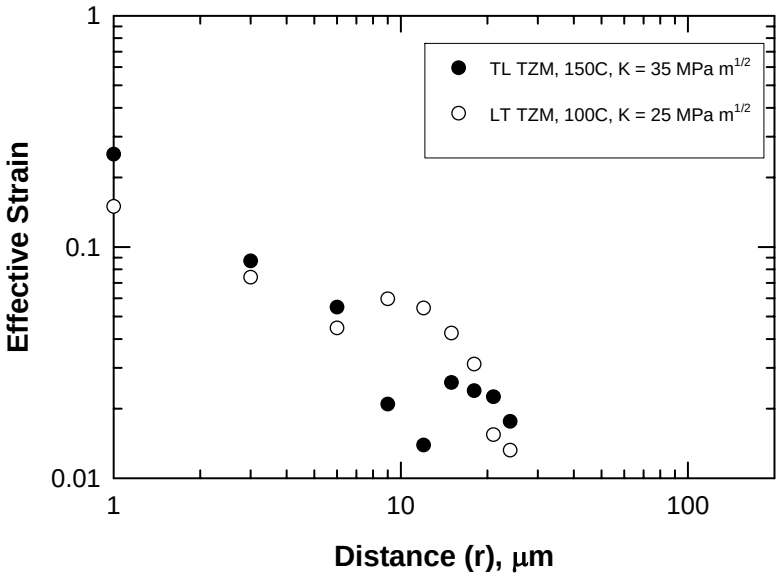

(c)

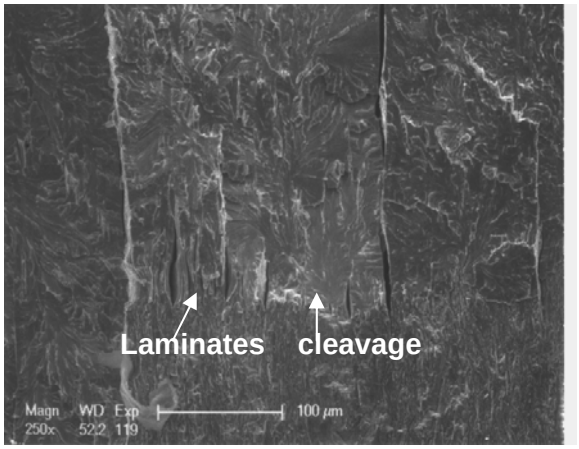

(d)

Figure 9. **Fracture process for TZM molybdenum: (a) SEM micrograph of the crack tip fracture process in the LT orientation tested at 100°C at K = 25 MPa $\sqrt{m}$, (b) crack tip for TL orientation tested at 150°C at K = 35 MPa $\sqrt{m}$, (c) crack tip effective strain distributions for LT and TL-TZM tested at 100°C and 150°C, respectively , and (d) fracture surface for LT-TZM after loading at 100°C to K = 30 MPa $\sqrt{m}$ showing a mixed-mode failure mechanism. The loading direction for Figs. 9a and 9b is horizontal, but the rolling direction is vertical for Fig. 9a and horizontal for Fig. 9b. The surface of the crack plane is shown in Fig. 9d that is perpendicular to the rolling direction.**

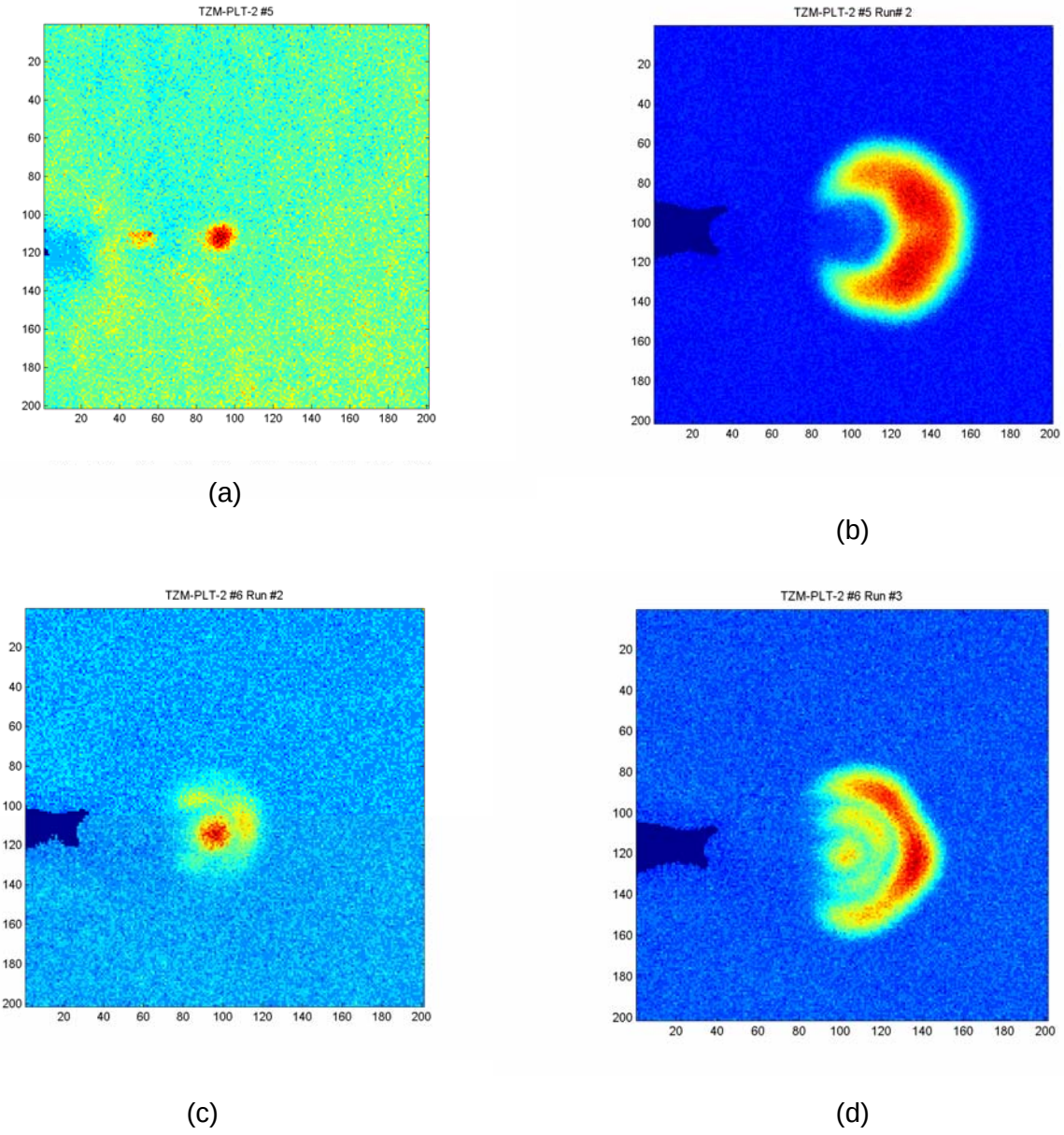

Figure 10. **Ultrasonic scan images of the crack tip from LT and TL-TZM molybdenum tested at 100°C and 150°C, respectively, showing the presence of internal delamination: (a) LT-TZM after pre-cracking, where the tensile K is estimated to be = 10 MPa $\sqrt{m}$, (b) LT-TZM after testing to K = 25 MPa $\sqrt{m}$, (c) TL-TZM after testing to K = 25 MPa $\sqrt{m}$, and (d) TL-TZM after testing to K = 35 MPa $\sqrt{m}$. Blue represents the intact region, while crack separation is highest in the red region, followed by yellow, and then light blue.**

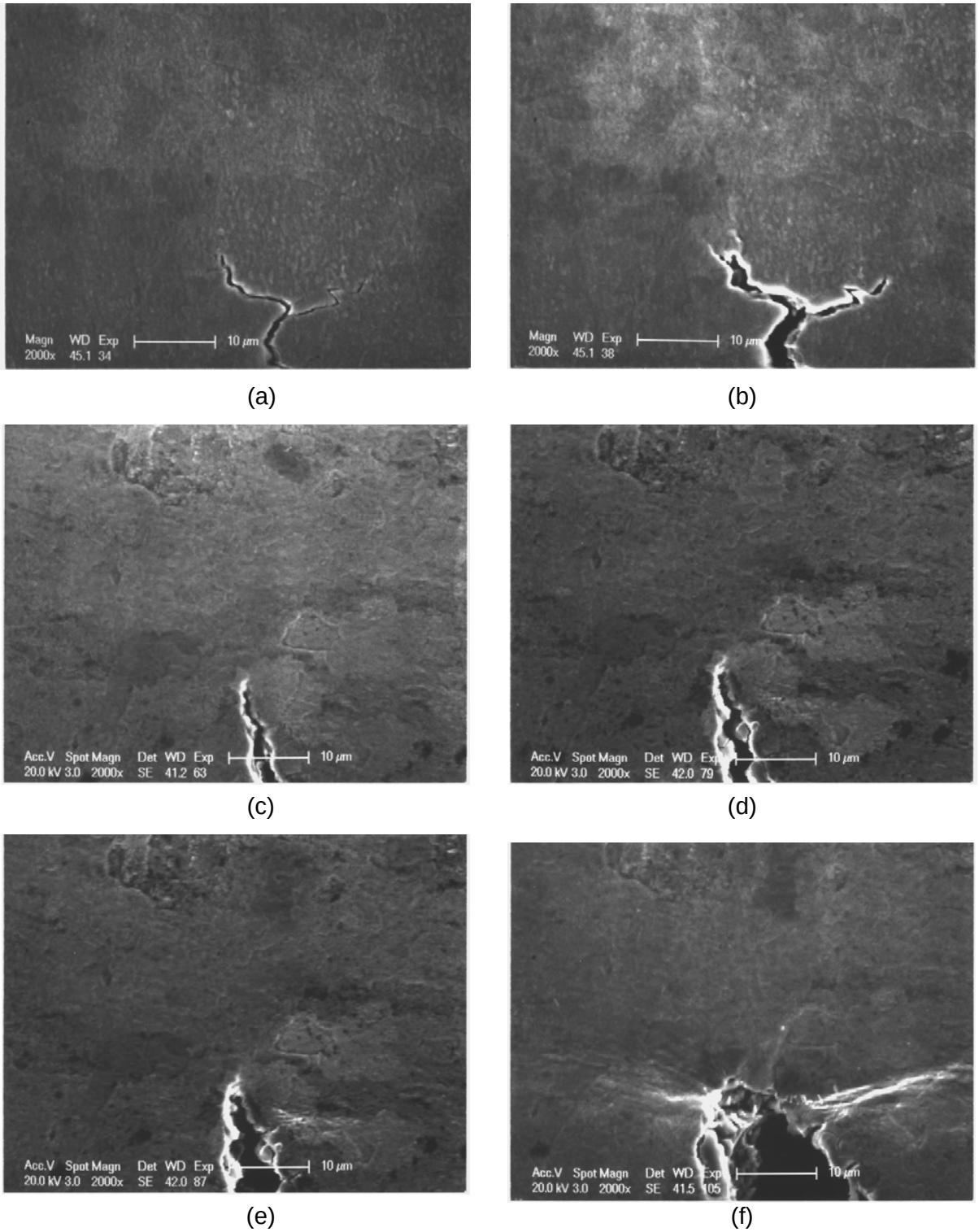

Figure 11. **SEM micrographs of the crack extension processes in LT-LCAC molybdenum tested at 150°C and 200°C at various K levels: (a) 150°C testing, K = 10 MPa$\sqrt{m}$ showing forked crack tips, (b) 150°C testing, K = 25 MPa$\sqrt{m}$ showing slipline emitted from one of the two crack tips, (c) 200°C testing, K = 30 MPa$\sqrt{m}$, (d) 200°C testing, K = 40 MPa$\sqrt{m}$, (e) 200°C testing, K = 50 MPa$\sqrt{m}$, and (f) 200°C testing, K = 55 MPa$\sqrt{m}$ showing extensive crack tip slip emission and crack opening with no crack extension. The loading direction and rolling direction is horizontal**.

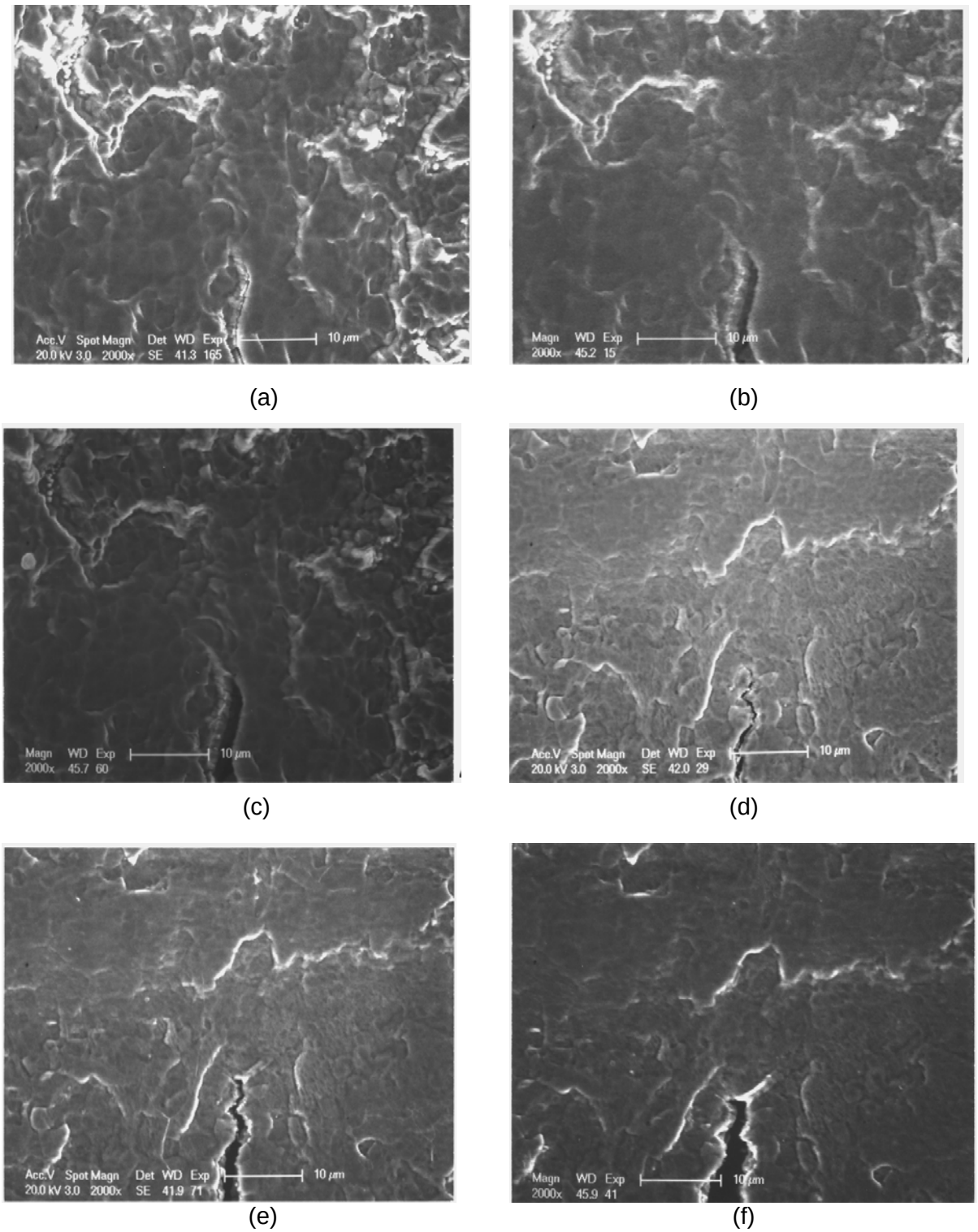

Figure 12. **SEM micrographs of the crack extension processes observed in TL-LCAC molybdenum for testing at 150°C and 200°C at various K-levels: (a) 150°C testing, K = 10 MPa$\sqrt{m}$, (b) 150°C testing, K = 35 MPa$\sqrt{m}$ showing slipline emission from the crack tip, (c) 150°C testing, K = 40 MPa$\sqrt{m}$, (d) 200°C testing, K = 20 MPa$\sqrt{m}$, (e) 200°C testing, K = 30 MPa$\sqrt{m}$ showing slipline emission at crack tip, and (f) 200°C testing, K = 70 MPa$\sqrt{m}$ showing crack opening and slipline emission without crack extension. The loading direction is horizontal. The rolling direction is vertical.**

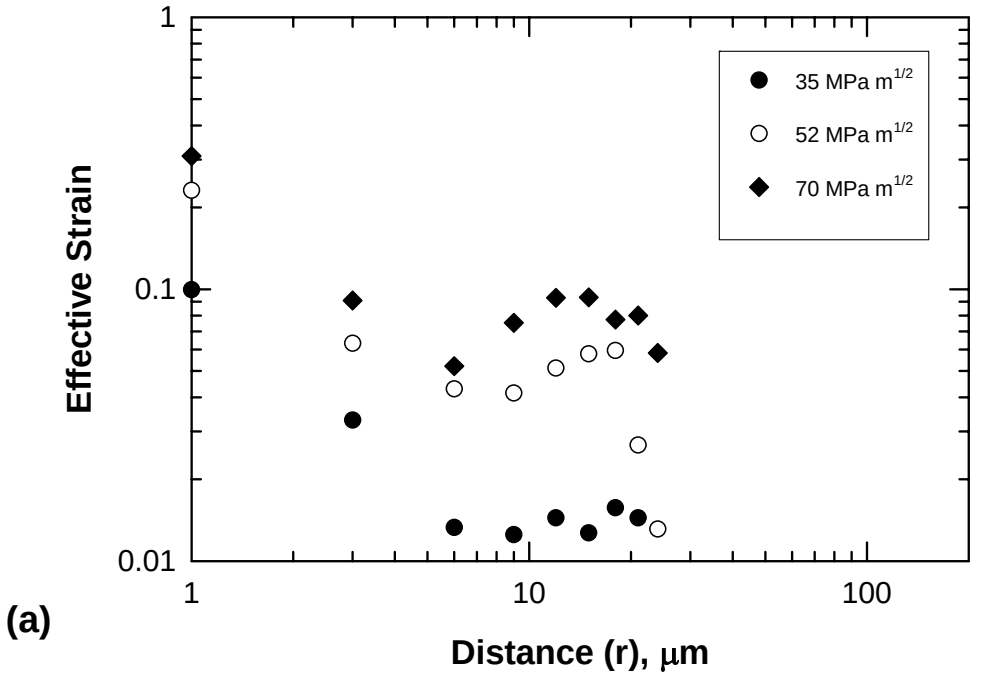

(a)

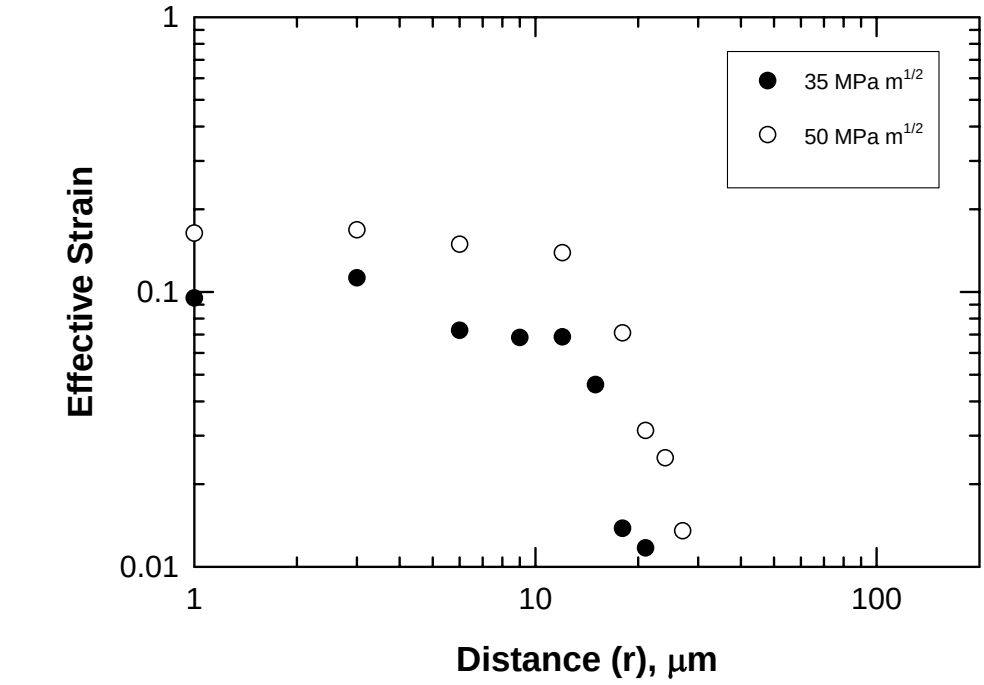

(b)

Figure 13. Near-tip strain distributions determined for LCAC molybdenum: (a) LT orientation tested at 200°C, and (b) TL orientation tested at 200°C.

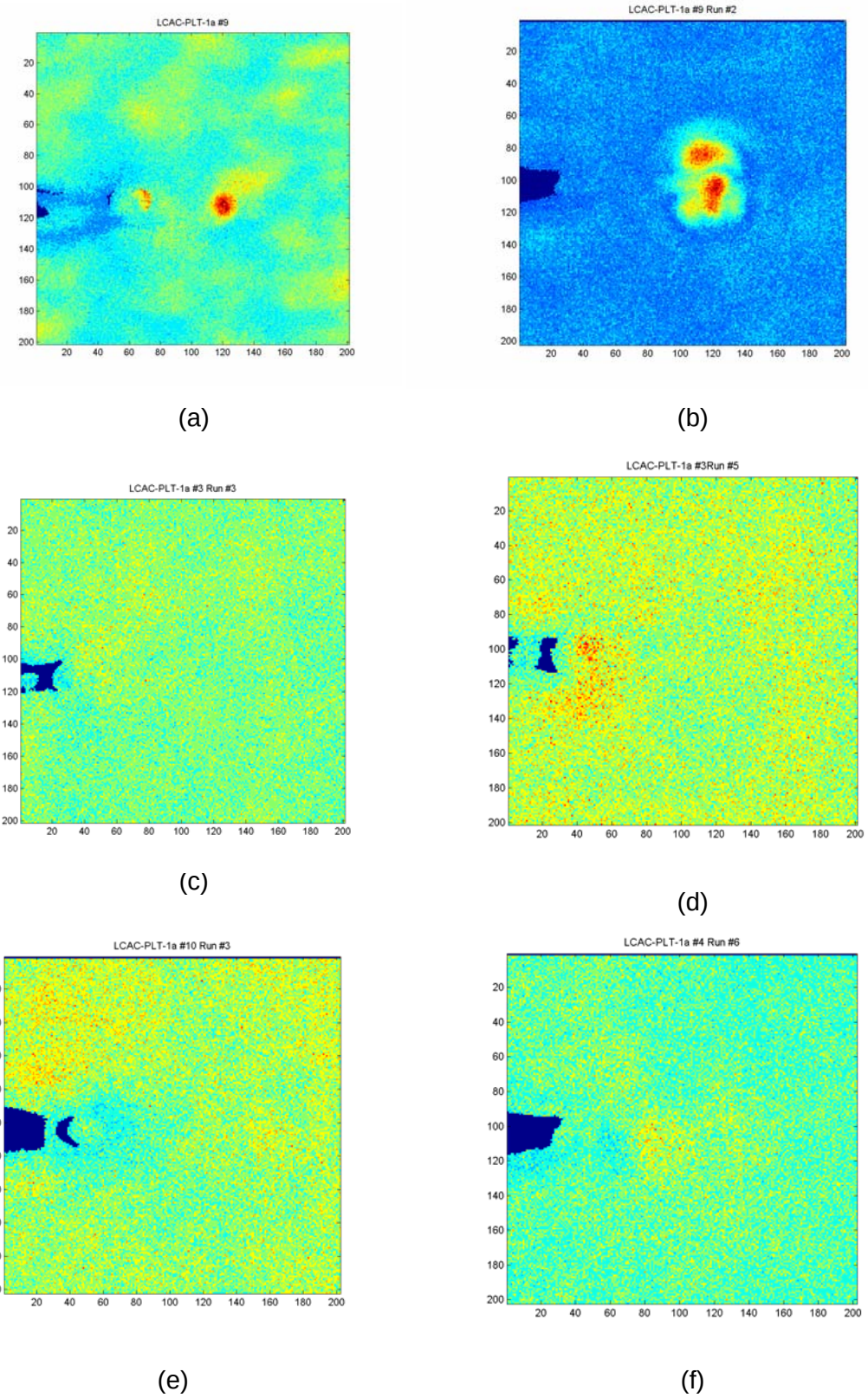

Figure 14. Ultrasonic scan images of the crack tip for LCAC molybdenum tested at 150°C to 200°C showing the presence of internal delamination: (a) TL tested at 150°C at K = 13 MPa $\sqrt{m}$, (b) TL tested at 150°C at K = 25 MPa $\sqrt{m}$ showing delamination zone, (c) TL tested at 200°C, K = 25 MPa $\sqrt{m}$, (d) TL tested at 200°C, K = 50 MPa $\sqrt{m}$, (e) LT tested at 150°C at K = 35 MPa $\sqrt{m}$ showing no delaminations, and (f) LT tested at 200°C at K = 70 MPa $\sqrt{m}$ with no delaminations resolved. Blue represents the intact region, while crack separation is highest in the red region, followed by yellow, and then light blue.

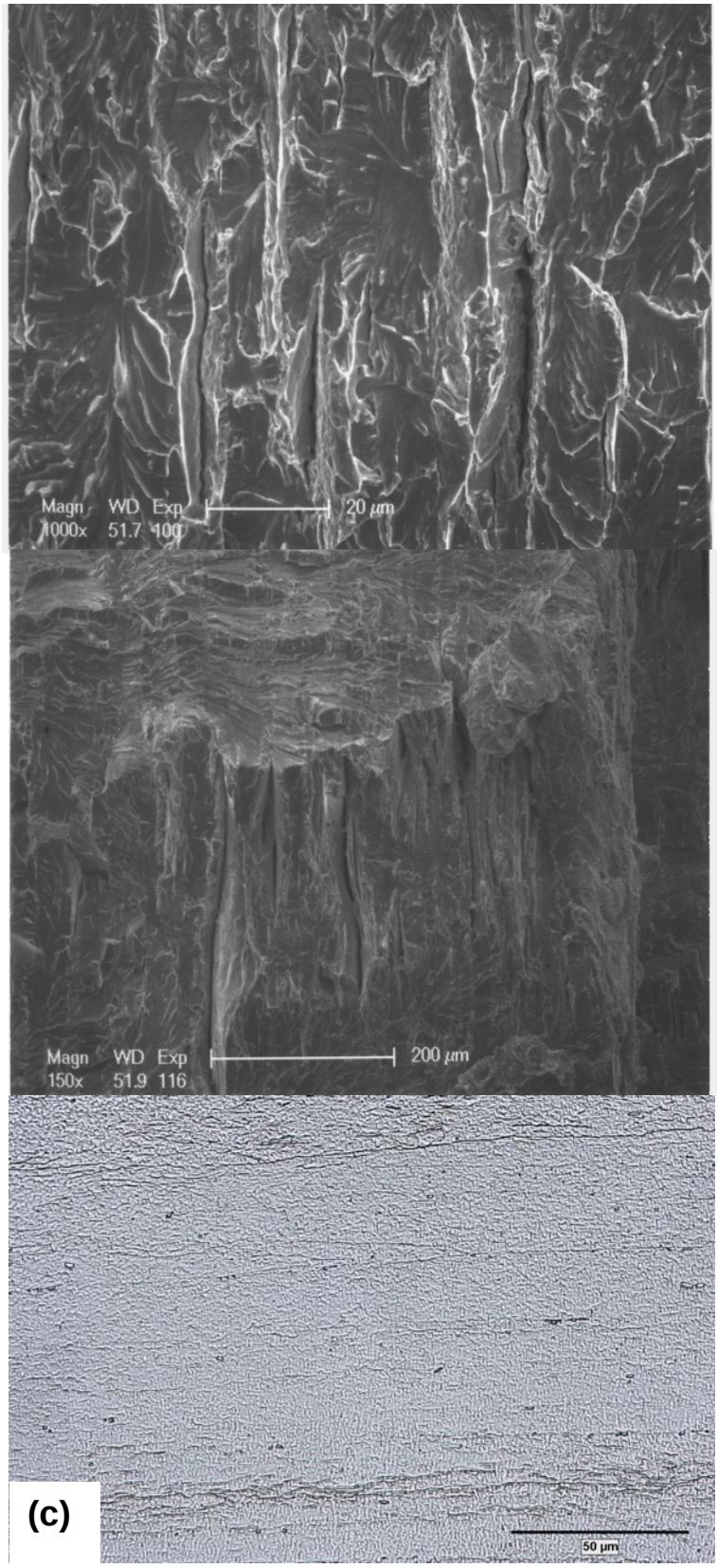

Figure 15. Fracture surfaces and metallographic sections at the crack tip for LCAC molybdenum specimens after testing: (a) fracture surface for TL-LCAC ODS tested at 150°C showing mixed mode cleavage and delaminations, (b) TL-ODS tested at 200°C showing the fracture surface with a mixed mode failure consisting of delaminations and laminates, and (c) metallographic section near the crack tip of LT-LCAC tested at 200°C where delamination cracks were not observed. The images for Fig. 15a and 15bd were taken from the plane perpendicular to the crack plane in the process zone ahead of the crack tip (Figure 16b). The surface of the crack plane is shown in Figs. 15a and 15b that is perpendicular to the rolling direction.

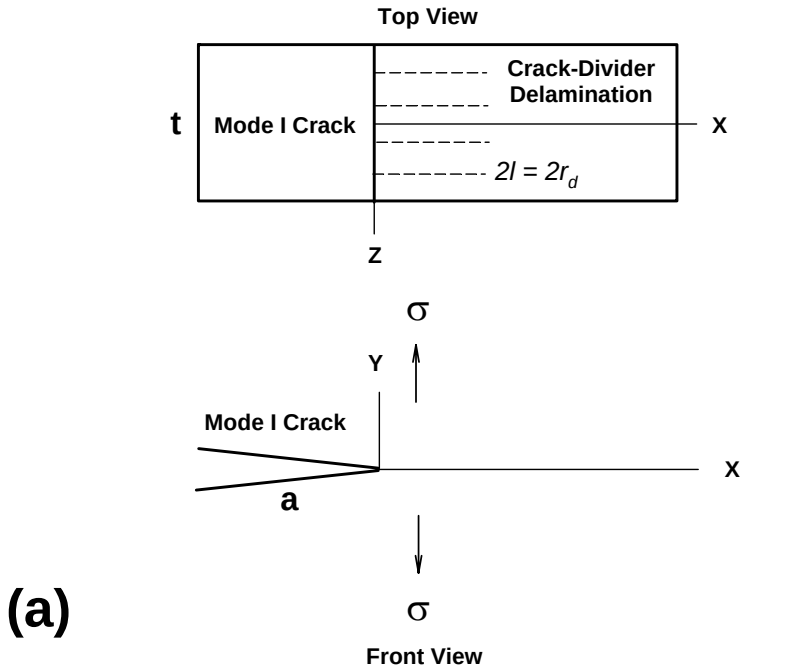

(a)

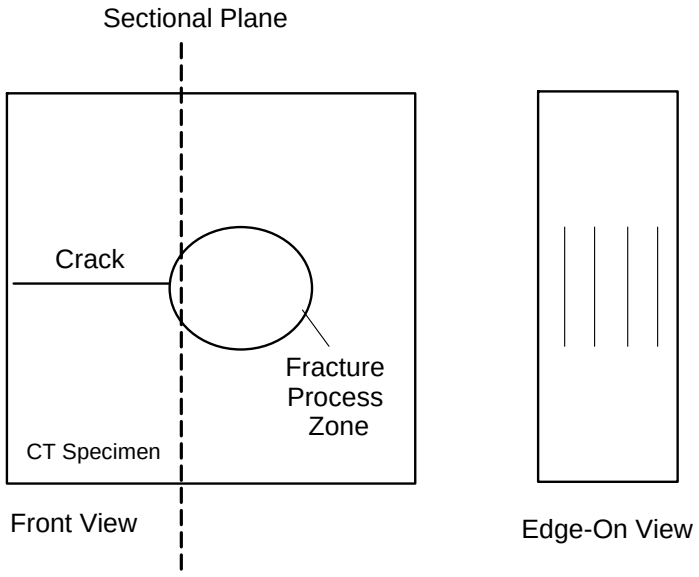

(b)

Figure 16. **Schematic shows the formation of thin-sheet ligaments: (a) used for model calculations in a plate of thickness t by crack-divider delamination in the crack tip plastic zone of a Mode I crack (crack length = a) subjected to a remote stress σ. The delamination zone is *l*, and (b) schematic of diagram used for sectioning.**

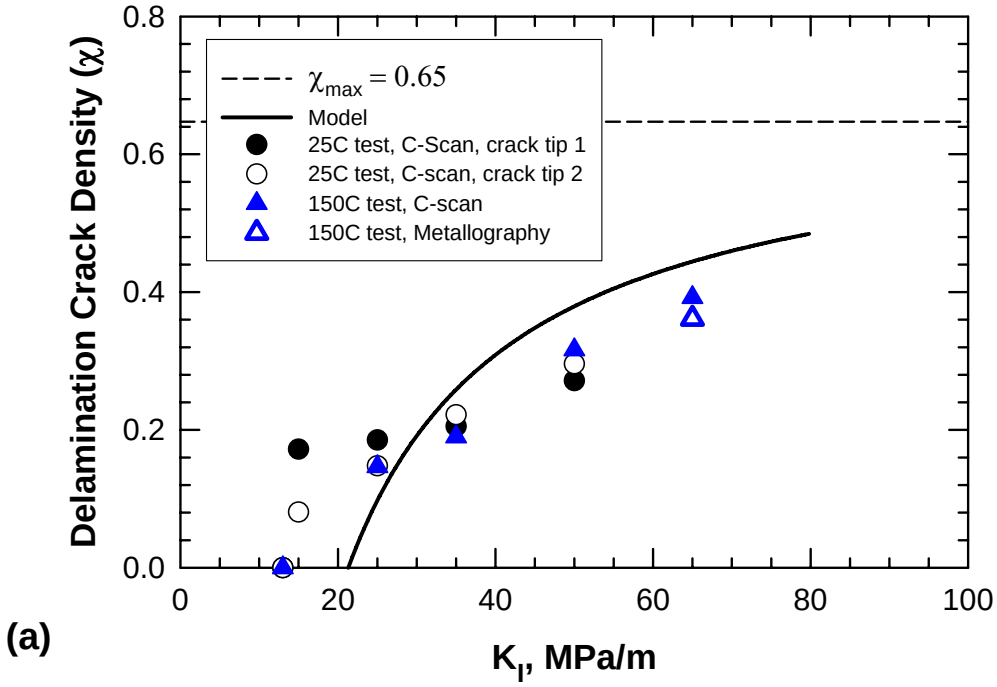

(a)

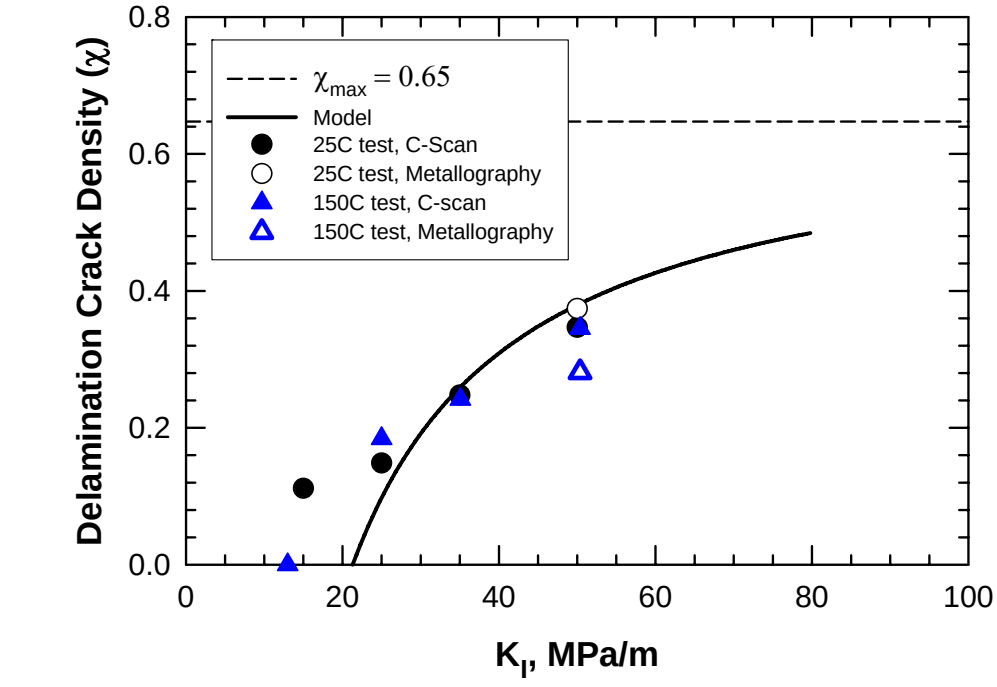

(b)

Figure 17. Values of crack density parameter, χ, determined from the measured delamination zone diameter (2 r_d) using Eq. (9) as a function of applied K for ODS molybdenum tested at room-temperature and 150°C compared with the model prediction (Eq (22)): (a) LT orientation, and (b) TL orientation. The model prediction was based on K_{IC}^{ST} = 10 MPa$\sqrt{\text{m}}$.

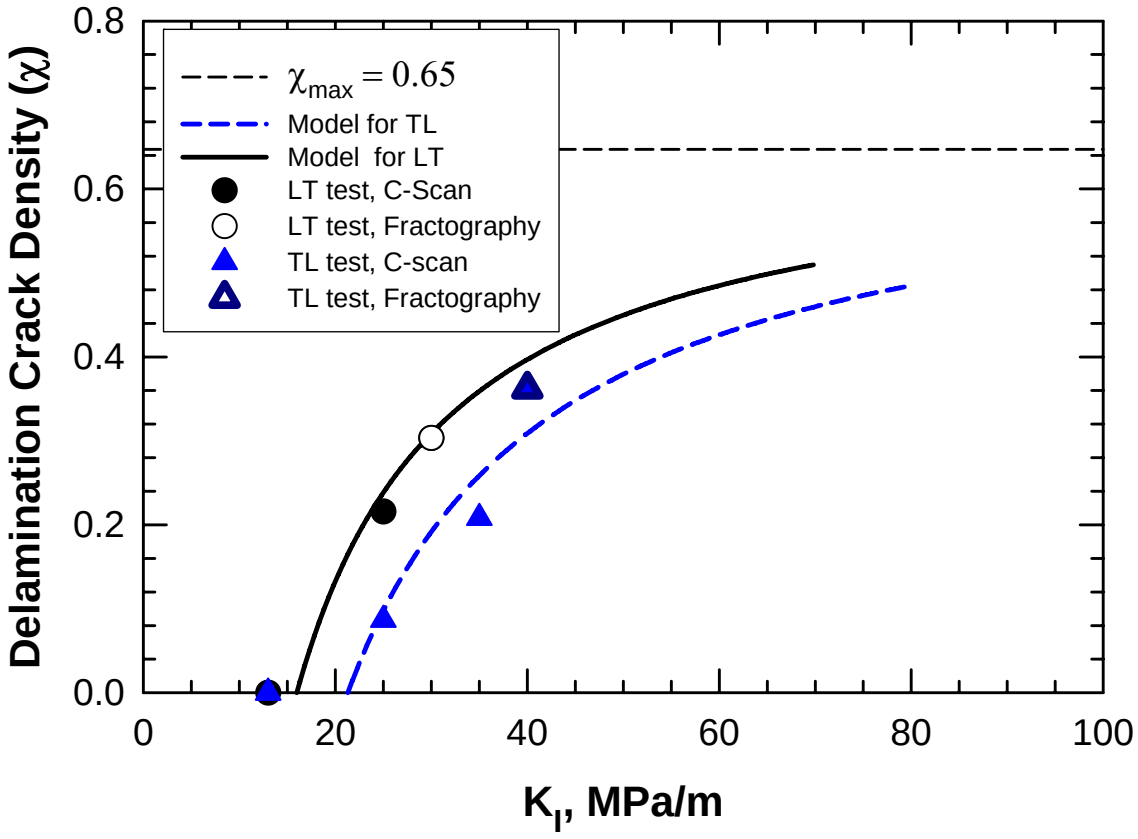

Figure 18. Values of crack density parameter, χ, determined from the measured delamination zone diameter (2 r_d) using Eq. (9) as a function of applied K for TZM molybdenum compared with the model prediction (Eq (22)) for the LT orientation tested at 100°C with the model prediction based on K_{IC}^{ST} = 7.5 MPa$\sqrt{\text{m}}$ and TL orientation tested at 150°C with a the model prediction was based on K_{IC}^{ST} = 10 MPa$\sqrt{\text{m}}$.

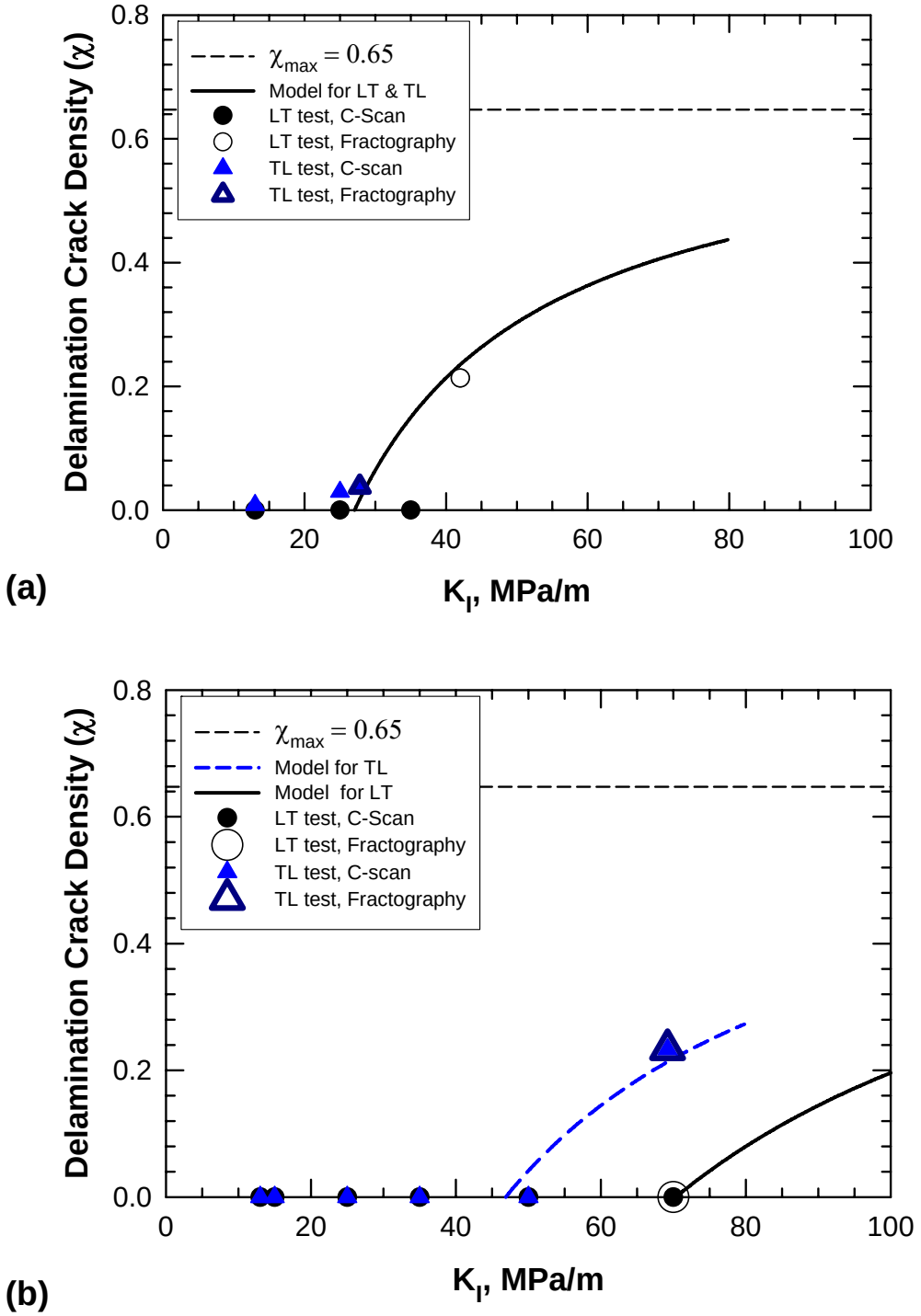

Figure 19. Values of crack density parameter, χ, determined from the measured delamination zone diameter (2 r_d) using Eq. (9) as a function of applied K for LCAC molybdenum tested at 150°C and 200°C compared with the model prediction (Eq (22)): (a) LT and TL orientation tested at 150°C with the model prediction based on K_{IC}^{ST} = 10 MPa$\sqrt{\text{m}}$, and (b) testing at 200°C for LT orientation with a model prediction was based on K_{IC}^{ST} = 33 MPa$\sqrt{\text{m}}$ (no delaminations were resolved) and TL orientation with a model prediction was based on K_{IC}^{ST} = 22 MPa$\sqrt{\text{m}}$.

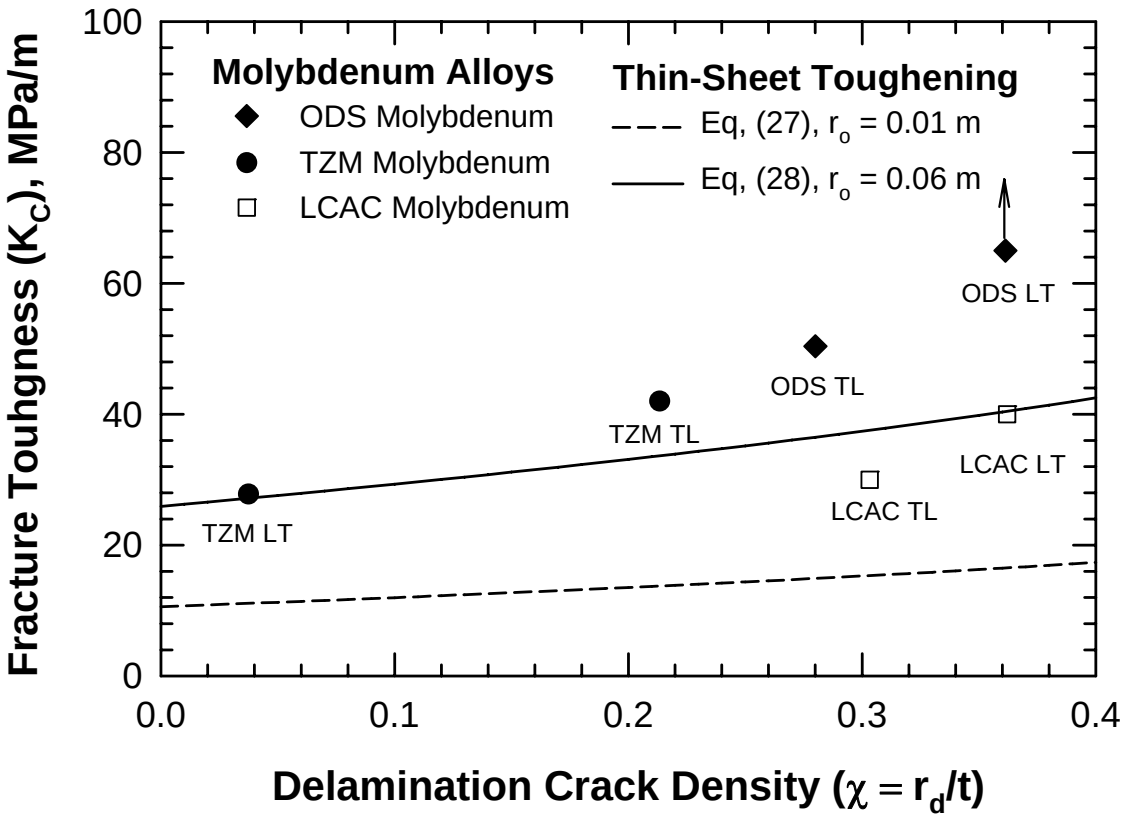

Figure 20. Correlation of fracture toughness (K_C) of Mo-based alloys with delamination crack density (χ) showing increasing K_C with increasing χ values.